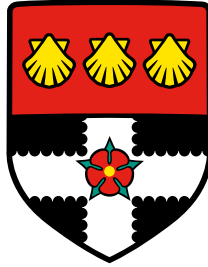


UNIVERSITY OF READING

Department of Meteorology



Representation of Mountains in Atmospheric Models

James Shaw

A dissertation submitted in partial fulfilment of the requirement for the degree of MSc Atmosphere
Ocean and Climate

August 2014

Abstract

A variety of methods exist to represent mountains in atmospheric models. The most common method in use today is that of terrain following layers. However, terrain following grids have the problem that, as model resolution increases, gradients in terrain tend to become steeper, which can lead to greater numerical errors.

An alternative to terrain following layers is the cut cell method. Cut cell grids are better able to represent steep slopes, but can result in very small cells that limit the model timestep unless the grid or the discretisation is modified to account for them. While each method offers potential advantages, cut cell grids have been found to give more accurate results in a limited number of test cases from the literature.

This project assesses the accuracy of terrain following and cut cell grids more rigorously using a wider set of two-dimensional test cases, using the same model for terrain following and cut cells. Two simulations are performed using a nonhydrostatic model and results are compared to those from the literature. First, spurious flow is analysed for an atmosphere at rest in the presence of an idealised mountain profile. Second, gravity waves are forced by horizontal flow over idealised orography. In addition, advection tests are performed to compare terrain following and cut cell grids. These include newly developed tests that are designed to challenge accuracy on cut cell grids.

We find that advection accuracy is greatest when advection follows grid layers. Advection is accurate in horizontal flows on cut cell grids since the grid is uniform aloft. There are modest errors on terrain following grids, but results are nonetheless more accurate than those from the literature. Results are accurate for terrain following flows on terrain following grids, but errors are significant on cut cell grids.

Spurious velocities are reduced in a resting atmosphere by using cut cell grid. However, in the gravity waves test, we find errors in potential temperature on the cut cell grid that are associated with the Lorenz computational mode.

We confirm results from previous studies that show that cut cells give good accuracy in certain test cases with flow or stratification that is aligned with the grid. However, we find that terrain following grids give reasonable accuracy in all test cases. Where flow interacts more significantly with the orography, as found in tests of gravity waves and terrain following advection, results are more accurate on terrain following grids than with cut cells.

Contents

1	Introduction	1
2	Theoretical basis	5
2.1	Coordinate transformations	5
2.2	Horizontal pressure gradient	7
2.3	Terrain following techniques	8
2.4	Cell shaving techniques	9
2.5	Finite volume method	10
2.6	Grid orthogonality, uniformity and skewness	11
2.7	Vertical staggering of variables	12
2.8	Gravity waves	13
3	Methodology	17
3.1	Grid construction	17
3.2	Discretisation of Euler equations	18
3.3	Energy measures	20
3.4	Courant–Friedrichs–Lewy criterion	21
4	Results	23
4.1	Horizontal tracer advection	23
4.2	Terrain following tracer advection	30
4.3	Resting atmosphere	32
4.4	Gravity waves	37
4.5	Terrain following advection of a stable thermal profile	45
5	Conclusions	49
6	Further work	51
6.1	Advection scheme	51
6.2	Resting atmosphere errors	52
6.3	Gravity waves and potential temperature errors	53
	Bibliography	55

1 Introduction

Orography has significant effects on local weather, creating strong downslope winds and enhancing local precipitation (Barry 2008). Large mountain ranges also affect global circulation. A mountain acts as a barrier to air flow and, due to conservation of vorticity, meridional displacement balances vortex stretching, giving rise to planetary waves which affect the development of pressure systems (Barry 2008). The Tibetan Plateau acts as an elevated heat source, raising temperatures and humidity in summer which help to maintain the Asian monsoon (Ye 1981; Luo and Yanai 1983). Terrain also affects global circulation by exerting low-level drag (Lott and Miller 1997) and transporting momentum via gravity waves (McFarlane 1987).

To capture these effects, numerical weather prediction (NWP) models must solve the equations of motion on a grid that represents the orography. Over flat ground the grid can be entirely regular, but in the presence of sloping terrain the grid must be modified. There are two main approaches: either transform the grid so that its vertical layers follow the terrain, or remove all or part of grid cells that intersect with the orography.

Terrain following (TF) layers are in widespread use in operational models and are usually implemented on a rectangular computational grid, using terrain following vertical coordinates instead of Cartesian coordinates. In this system, the terrain's influence decays with height: the bottommost layers follow the underlying surface closely while the uppermost layers are flat.

It is well-known that TF coordinates perform badly in the presence of steep orography (Gary 1973). As spatial resolution in NWP models increases, gradients in terrain tend to become steeper (Steppeler et al. 2002). This leads to larger truncation errors in calculating the horizontal pressure gradient which result in spurious winds (Dempsey and Davis 1998). Much work has been done to reduce error associated with TF coordinates: firstly, by smoothing the effects of terrain with height (Simmons and Burridge 1981; Schär et al. 2002; Leuenberger et al. 2010; Klemp 2011) and, secondly, by improving the accuracy in calculating the horizontal pressure gradient itself (Mahrer 1984; Klemp 2011; Zängl 2012).

Despite their associated numerical errors, TF coordinates are attractive because their rectangular structure is simple to process by computer, boundary layer resolution can be increased with variable spacing of vertical layers (Schär et al. 2002), and cell sizes remain almost constant (Jebens et al. 2011).

An alternative to terrain following layers is to 'shave', or 'cut', cells where they intersect with the

terrain surface. Cells that lie entirely below the terrain are removed, and those that intersect the surface are modified in shape so that they more closely fit the terrain. This modification means that some cells become very small, which can reduce computational efficiency (Klein et al. 2009), and several approaches have been tried to alleviate the problem (Steppeler et al. 2002; Yamazaki and Satomura 2010; Jebens et al. 2011).

Several studies found that cut cells produce more accurate results when compared to TF coordinates. Spurious winds seen in TF coordinates are not present and errors do not increase with steeper terrain (Good et al. 2014). A comparison of TF and cut cells using real initial data by Steppeler et al. (2006) found that precipitation patterns, temperature and wind fields were forecast more accurately in the cut cell model.

Other representations of terrain have been developed using unstructured grids (Smolarkiewicz and Szmelter 2011; Pain et al. 2005). They are able to represent the boundary accurately, but more complex discretisations are required to maintain accuracy because the mesh is not aligned with the dominant vertical force of gravity (Rosatti et al. 2005), just as horizontal pressure gradients are difficult to calculate in TF coordinates.

Unstructured grids can be combined with dynamic mesh adaptation so that small scale features can be resolved in areas of interest, such as regions of frontogenesis, inversion layers, and the boundary layer (Browne et al. 2014). Dynamically adaptive meshes reduce the number of grid cells needed to represent small scale features, but updating the mesh can take a significant amount of computation time (Blaise and St-Cyr 2012; Browne et al. 2014). Furthermore, mesh adaptation does not necessarily lead to a more accurate model (Parkinson et al. 2014).

Project outline

This project aims to compare the accuracy of TF and cut-cell style grids in a variety of two-dimensional test cases. Simulations are performed using the OpenFOAM CFD library (OpenCFD Foundation 2014b) with a finite volume discretisation of the fully compressible Euler equations from Weller and Shahrokhi (2014). The model includes a curl-free pressure gradient formulation, an upwind-biased cubic advection scheme, and a Lorenz vertical staggering of variables. All tests are performed using the same model on TF and cut cell style grids, enabling like-for-like comparison between grids.

In chapter 2, the theory of coordinate transforms is introduced and applied to a discretisation of the horizontal pressure gradient. We review the main types of terrain following transformations and present three shaving techniques used to construct cut cell grids. The finite volume method, grid skewness, and the Lorenz and Charney–Phillips vertical staggarings are outlined. We end the chapter with a brief description of the linear theory of gravity waves that is later used to evaluate experimental results.

In chapter 3, we describe the method of grid construction using the OpenFOAM CFD library. An overview of the model discretisation from Weller and Shahrokhi (2014) is given and its curl-free pressure gradient and upwind-biased cubic advection scheme are described. The chapter concludes

by describing the calculation of energy measures and the Courant–Friedrichs–Lewy criterion on an unstructured grid.

The results of five experiments are discussed in chapter 4. Results of three standard test cases are compared with results from the literature, and two new test cases are developed which shed light on some problems with cut cells. The first two tests challenge the upwind-biased advection scheme. The first, standard test transports a tracer in a horizontal flow. The second test is formulated to find the cause of errors in the horizontal advection test by transporting a tracer in a terrain following flow. The third test examines spurious motion in a resting atmosphere in the presence of orography. The fourth test generates orographically induced gravity waves and errors in potential temperature found on the cut cell style grid are discussed. A final test is developed to investigate the cause of these errors by advecting a stable thermal profile.

Concluding remarks on the experimental results are made in chapter 5. Finally, areas of further work are discussed in chapter 6. Additional tests are suggested to explore the source of numerical errors that were found in the experimental results. In particular, we recommend the formulation of a new Charney–Phillips staggering on unstructured grids. We hope that, by modifying the model to use this staggering, numerical error would be reduced.

2 Theoretical basis

In this chapter, we review the theory that underpins the construction of the TF grids, cut cell grids, and discretisation techniques that are used in this project. First, we present the theory of coordinate transformation, commonly used in terrain following layers, and demonstrate how it can be applied to a forward-in-space discretisation of a horizontal pressure gradient. We go on to review the origins of terrain following coordinates and more recent refinements to terrain following grids. Next, the cut cell method is described. We outline the ‘small cell’ problem that is inherent with the cut cell method and explain some approaches that address it.

After outlining the finite volume discretisation method that is used by the model for this project, we discuss grid orthogonality, uniformity and skewness and their impact on numerical accuracy. Next, we outline the two most common vertical staggers of variables: the Charney–Phillips grid and the Lorenz grid. The chapter concludes with a review of linear wave theory, giving examples of the structure of stationary waves over infinite sinusoidal hills.

2.1 Coordinate transformations

A model implementation that uses terrain following layers must choose from a variety of vertical coordinates. The equations of motion with the hydrostatic approximation are simplified by using pressure coordinates (Eliassen 1949). However, because pressure varies in the horizontal, the lower boundary condition becomes complicated because surfaces of constant pressure intersect the terrain. This motivated Phillips (1957) to create the sigma coordinate in which pressure is normalised such that σ ranges between zero at the top of the domain, and one at the surface. Most hydrostatic models use normalised pressure coordinates. With some exceptions, such as Xue and Thorpe (1991), nonhydrostatic models use height-based coordinates (Steppeler et al. 2003).

Isentropic coordinates have also been investigated. Since adiabatic motion follows isentropic surfaces, errors in discretising vertical advection are negligible. However, difficulties arise when isentropes intersect with the surface (Konor and Arakawa 1997).

Typically, terrain following models use transformed height or pressure coordinates so that the computational domain becomes rectangular. Consider the two-dimensional Cartesian coordinates (x, z)

and transformed coordinates (x^*, z^*) . The transformation functions must be monotonic so that the transformation is invertible.

A scalar field, φ , can be expressed in transformed coordinates as $\varphi(x^*, z^*)$ or in Cartesian coordinates as $\varphi(x^*(x), z^*(x, z))$. Hence the vertical derivative of φ can be found by using the chain rule (Marshall et al. 2004)

$$\frac{\partial \varphi}{\partial z} = \frac{\partial \varphi}{\partial z^*} \frac{\partial z^*}{\partial z} \quad (2.1)$$

The multivariable chain rule is needed to find the horizontal derivative. Given two sets of functions

$$\begin{aligned} y_1 &= y_1(u_1, \dots, u_j) \\ &\vdots \\ y_i &= y_i(u_1, \dots, u_j) \end{aligned}$$

and

$$\begin{aligned} u_1 &= u_1(x_1, \dots, x_k) \\ &\vdots \\ u_j &= u_j(x_1, \dots, x_k) \end{aligned}$$

we can apply a $i \times k$ Jacobi rotation matrix (Apostol 1969)

$$\frac{\partial y_i}{\partial x_k} = \begin{bmatrix} \frac{\partial y_1}{\partial x_1} & \frac{\partial y_1}{\partial x_2} & \dots & \frac{\partial y_1}{\partial x_k} \\ \vdots & \vdots & \ddots & \vdots \\ \frac{\partial y_i}{\partial x_1} & \frac{\partial y_i}{\partial x_2} & \dots & \frac{\partial y_i}{\partial x_k} \end{bmatrix} \quad (2.2)$$

where y_i and x_k are first-order tensors with i and k covariant indices respectively. Similarly, defining the tensors $\partial y_i / \partial u_j$ and $\partial u_j / \partial x_k$ then we can express the chain rule as

$$\frac{\partial y_i}{\partial x_k} = \frac{\partial y_i}{\partial u_j} \frac{\partial u_j}{\partial x_k} \quad (2.3)$$

using the convention that repeated indices imply summation. Applying this to φ we find

$$\left[\frac{\partial \varphi}{\partial x} \quad \frac{\partial \varphi}{\partial z} \right] = \left[\frac{\partial \varphi}{\partial x^*} \quad \frac{\partial \varphi}{\partial z^*} \right] \begin{bmatrix} \frac{\partial x^*}{\partial x} & \frac{\partial x^*}{\partial z} \\ \frac{\partial z^*}{\partial x} & \frac{\partial z^*}{\partial z} \end{bmatrix} \quad (2.4)$$

and the horizontal component of equation 2.4 is then

$$\frac{\partial \varphi}{\partial x} \Big|_z = \frac{\partial \varphi}{\partial x^*} \frac{\partial x^*}{\partial x} \Big|_{z^*} + \frac{\partial \varphi}{\partial z^*} \frac{\partial z^*}{\partial x} \Big|_z \quad (2.5)$$

where the subscript by the vertical bar denotes the variable that is held constant. With terrain following methods, only the vertical coordinate is transformed. Since there is no horizontal transformation, $x = x^*$, and equation 2.5 simplifies to

$$\left. \frac{\partial \varphi}{\partial x} \right|_z = \left. \frac{\partial \varphi}{\partial x} \right|_{z^*} + \frac{\partial \varphi}{\partial z^*} \left. \frac{\partial z^*}{\partial x} \right|_z \quad (2.6)$$

In a two-dimensional terrain-following coordinate transform, there is the added requirement that the transformed domain be rectangular. This can be satisfied by imposing boundary conditions (Schär et al. 2002)

$$z^*(x, h(x)) = 0 \quad , \quad z^*(x, H) = H \quad (2.7)$$

where H is the height of the domain and $h(x)$ is the height of the terrain surface.

2.2 Horizontal pressure gradient

In models that use TF coordinates, the horizontal pressure gradient can be calculated in the transformed coordinate system. It follows from equation 2.6 that, in TF coordinates, the horizontal gradient of pressure p is (Mahrer 1984)

$$\left. \frac{\partial p}{\partial x} \right|_z = \left. \frac{\partial p}{\partial x} \right|_{z^*} + \frac{\partial z^*}{\partial x} \left. \frac{\partial p}{\partial z^*} \right|_z \quad (2.8)$$

The first term on the right hand side is the change in pressure along the TF coordinate surface, and the second term corrects for the vertical variation in the first. These terms tend to be large and of opposite sign over steep terrain, and a discretisation must be at least first order accurate so that the difference between the hydrostatic components of the two terms converges to zero (Gary 1973).

A first-order forward difference approximation of the horizontal pressure gradient can be found from equation 2.8, such that

$$\left. \frac{\partial p}{\partial x} \right|_z = \frac{P_{i+1,k} - P_{i,k}}{\Delta x} + \frac{\partial z^*}{\partial x} \frac{P_{i+1,k} - P_{i+1,k-1}}{\Delta z^*} + \mathcal{O}(\Delta x) \quad (2.9)$$

Errors in the horizontal pressure gradient are associated with horizontal acceleration by the momentum equation, and have been shown to generate spurious winds (Klemp et al. 2003; Klemp 2011).

Errors can be reduced by improving the accuracy of the horizontal pressure gradient discretisation. Mahrer (1984) proposed a discretisation where two pressure values at the same geometric height are interpolated from surrounding points. From these values, a horizontal pressure gradient can be calculated without introducing metric terms. Recent studies have found that variations of Mahrer's technique reduce spurious circulations (Dempsey and Davis 1998; Klemp 2011; Zängl 2012). It is interesting to note that, in order to improve accuracy in calculating the horizontal pressure gradient, these authors have abandoned the metric terms and calculated the horizontal pressure gradient more directly.

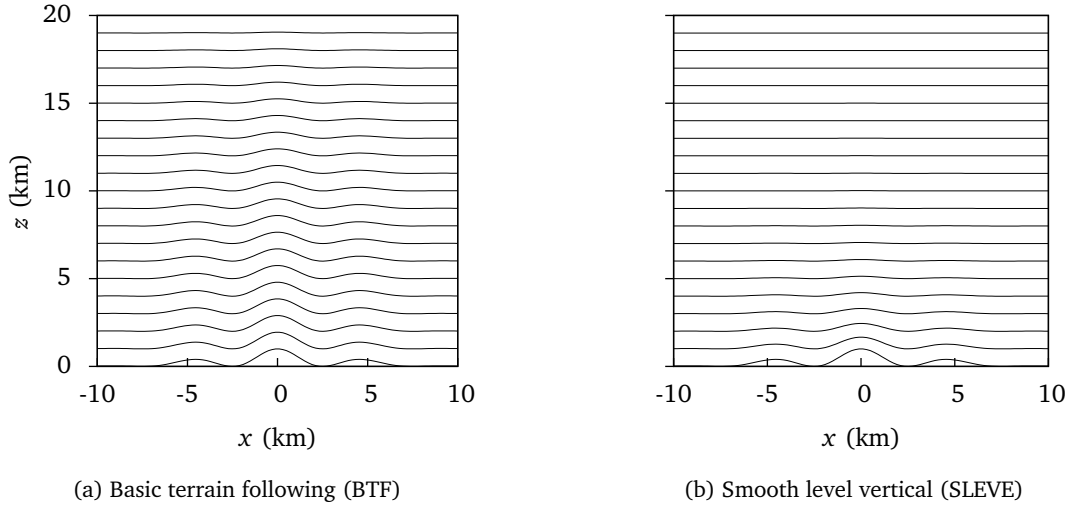


Figure 2.1: Example vertical cross sections of terrain following layers illustrating the decay in terrain influence with height. In BTF the decay is linear; in SLEVE it is exponential.

2.3 Terrain following techniques

As well as improving discretisation accuracy, errors due to coordinate transformation can also be reduced by smoothing the effect of the terrain so that the grid becomes more regular aloft.

Gal-Chen and Somerville (1975) proposed a basic terrain following (BTF) coordinate system in which the terrain's influence decays linearly with height but disappears only at the top of the domain (example shown in figure 2.1a). The transformation is defined as

$$z^* = H \frac{z - h}{H - h} \quad (2.10)$$

or

$$z = (H - h) \frac{z^*}{H} + h \quad (2.11)$$

where, in two dimensions, $z(x, z^*)$ is the height of the coordinate surface at level z^* , H is the height of the domain, and $h(x)$ is the height of the terrain surface.

The sigma coordinate transform of Phillips (1957) is equivalent to the BTF coordinate transform since they both decay linearly. However, since they decay with pressure rather than height, sigma coordinates also change with horizontal variations in pressure.

The hybrid terrain following (HTF) coordinates of Simmons and Burridge (1981) improve upon BTF coordinates by allowing the vertical decay profile can be controlled. By choosing a suitable profile, terrain influence decays more rapidly than BTF to produce surfaces of constant height aloft (Klemp 2011).

The coordinate system can be further refined by decaying small-scale features more rapidly than large-scale features to produce smooth coordinate surfaces in the middle and top of the domain. Schär

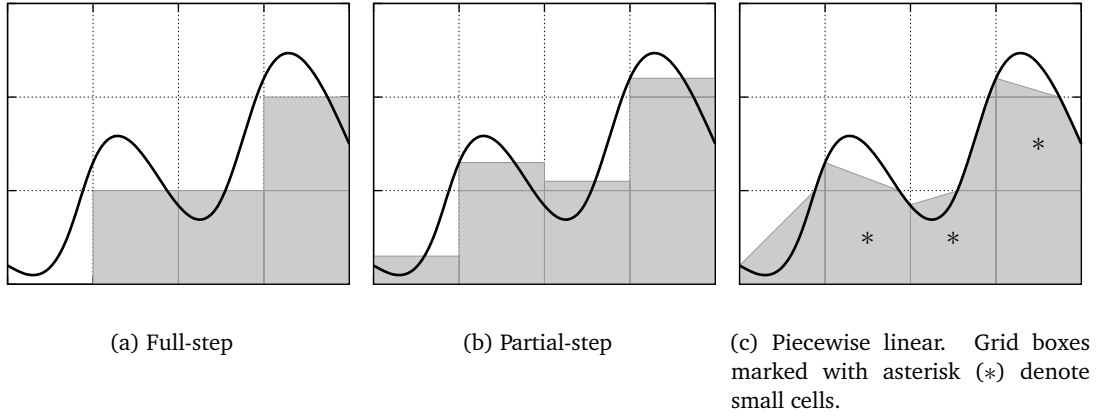


Figure 2.2: Vertical cross sections illustrating different methods of shaving cells intersecting with a hypothetical surface (heavy line). Adapted from Adcroft et al. (1997).

et al. (2002) achieved this with smooth level vertical (SLEVE) coordinates in which terrain height is split into a large-scale component h_1 and a small-scale component h_2 such that $h = h_1 + h_2$. Each component has a different exponential decay profile. The transformation is defined as

$$z = z^* + h_1 b_1 + h_2 b_2 \quad (2.12)$$

with the vertical decay functions are given by

$$b_i = \frac{\sinh((H - z^*)/s_i)}{\sinh(H/s_i)} \quad (2.13)$$

where s_1 and s_2 are the scale heights of large-scale and small-scale terrain respectively. SLEVE produces smooth coordinate surfaces in the middle and top of the domain (see figure 2.1b).

Leuenberger et al. (2010) generalised the SLEVE transformation in order to increase cell thickness in the layers nearest the ground, allowing longer timesteps and permitting more accurate calculation of parameterised low-level heat and momentum fluxes. An exponent n is introduced so that the generalised decay functions become

$$b_i = \frac{\sinh((H/s_i)^n - (z^*/s_i)^n)}{\sinh(H/s_i)^n} \quad (2.14)$$

where the optimal exponent value was found to be $n = 1.35$.

In the smoothed terrain following (STF) coordinate, Klemp (2011) took an alternative approach, using a multipass smoothing operator, and found that errors were reduced still further compared to SLEVE.

2.4 Cell shaving techniques

Mesinger et al. (1988) proposed a grid that, like terrain following grids, retains almost-constant cell sizes. The step-mountain (or ‘full-step’) coordinate removes cells that are intersected by the terrain so

creating steps over the surface (see figure 2.2a). Gallus and Klemp (2000) found that lee slope winds are too weak over smooth orography, but this study did not examine performance over steep terrain. In contrast, Mesinger (2004) compared results from three operational NCEP models that suggested the step-coordinate model was more skillful than the TF coordinate models in forecasting precipitation over the mountainous western United States.

Adcroft et al. (1997) proposed a partial-step system for modelling the ocean surface in which the cell height is adjusted so that cell volume is accurately represented (figure 2.2b). Compared to the full-step approach of Mesinger et al. (1988), spurious oscillations were significantly reduced advecting a tracer over topography.

The piecewise linear cut cell method is another alternative to terrain following layers. Here, the surface terrain is intersected with a regular Cartesian grid such that cells are cut where they intersect with the ground. This leads to cells that are entirely above the surface, entirely below it, and those which intersect with the ground. Those cells which intersect the ground have, in two dimensions, a triangular, trapezoidal or pentagonal shape (Rosatti et al. 2005). Figure 2.2c shows an example of this method. In some grid boxes, small cells, marked with an asterisk (*), are created by intersection with the surface. The primary difficulty is with numerical stability and reduced model efficiency associated with small cells. Additionally, because vertical resolution varies at the mountain top, this non-uniformity leads to second-order accurate schemes becoming only first-order accurate (grid uniformity is discussed in section 2.6).

A variety of solutions to the ‘small cell problem’ have been proposed. In Yamazaki and Satomura (2010), small cells are combined with horizontally or vertically adjacent cells. Steppeler et al. (2002) use a ‘thin-wall’ approximation to increase the computational volume of small cells without altering the terrain. Conceptually, each cell partially or completely below the mountain is filled with air and surrounded by a thin wall. Where a cell is cut by the terrain, the computational volume is equal to that of an uncut cell. Jebens et al. (2011) avoid the timestep restriction associated with explicit schemes by using an implicit method for cut cells and a semi-explicit method elsewhere.

2.5 Finite volume method

The finite volume method is a discretisation technique that represents the spatial domain as a non-overlapping grid of cells with fields represented as piecewise constant in each cell. At each timestep, cell averages are updated by considering the flux \mathbf{F} across the faces of the cell surface. In atmospheric modelling, \mathbf{F} is typically the advective flux, $\mathbf{u}\varphi$, where \mathbf{u} is the velocity field.

The notation used in this project for the representation of discrete variables follows Weller and Shahrokhi (2014). A cell average of φ is written as φ_c , where c denotes a cell. A scalar field, ψ , located at a face is written as ψ_f , where f denotes a cell face. An interpolation of cell centre averages of φ onto a face f is written as φ_f . $f \in c$ represents the faces of a cell. $c \in f$ represents the cells c that share a face f .

To describe the finite volume method, we start by considering the conservation of φ

$$\frac{\partial \varphi}{\partial t} + \nabla \cdot (\mathbf{u} \varphi) = 0 \quad (2.15)$$

Taking the volume integral over a cell c with volume \mathcal{V}_c we find

$$\int_{\mathcal{V}_c} \frac{\partial \varphi}{\partial t} d\mathcal{V} + \int_{\mathcal{V}_c} \nabla \cdot (\mathbf{u} \varphi) d\mathcal{V} = 0 \quad (2.16)$$

Integrating the first term gives the cell average φ_c and applying the divergence theorem to the second term gives a surface integral, hence

$$\mathcal{V}_c \frac{\partial \varphi_c}{\partial t} + \int_{S_c} \varphi \mathbf{u} \cdot \hat{\mathbf{n}} dS = 0 \quad (2.17)$$

where S_c is the cell surface area and $\hat{\mathbf{n}}$ is the unit vector that is outward normal to the surface. Dividing by the cell volume and, for a cell with a finite number of surfaces, this becomes

$$\frac{\partial \varphi_c}{\partial t} + \frac{1}{\mathcal{V}_c} \sum_{f \in c} \varphi_f \mathbf{u}_f \cdot \hat{\mathbf{n}} S_f = 0 \quad (2.18)$$

where S_f is the surface area of face f , and φ_f is the interpolated value of φ at the face. This interpolation of cell averages onto faces is a significant source of truncation error in finite volume systems (Adcroft et al. 1997).

The finite volume method often leads to a staggering of variables with fluxes at cell faces. Because cell averages are modified only through surface fluxes, a quantity of φ that fluxes out of one cell must flux into another. Thus, φ is conserved in the finite volume method.

2.6 Grid orthogonality, uniformity and skewness

A grid without orography may be orthogonal, uniform, and have no skewness, and these properties simplify the spatial discretisation. However, in the presence of terrain, most methods alter the shape of grid cells to better represent the surface. With the exception of the full-step shaving method, these cell modifications will affect orthogonality, uniformity and skewness.

A uniform grid is one in which cell dimensions are uniform (LeVeque 2002). On a x - z plane, this means that Δx and Δz are constant. When linearly interpolating onto a cell face, a uniform grid results in second-order accuracy because the centre of the face is equidistant from the two adjoining cell centres. On a non-uniform grid, the interpolation becomes first-order accurate.

A grid is orthogonal when angles between cell vertices are 90° ; that is, when cells are rectangular. Piecewise linear cut cell grids are orthogonal everywhere except where cells intersect the ground, whereas terrain following grids tend to have greater non-orthogonality.

Non-orthogonality typically causes skewness, which is created by the misalignment of cell faces with adjoining cell centres. Consider a two dimensional grid having two cells, c_1 and c_2 that share a common face f having vertices p_1 and p_2 . Skewness is defined as the distance between the centre of

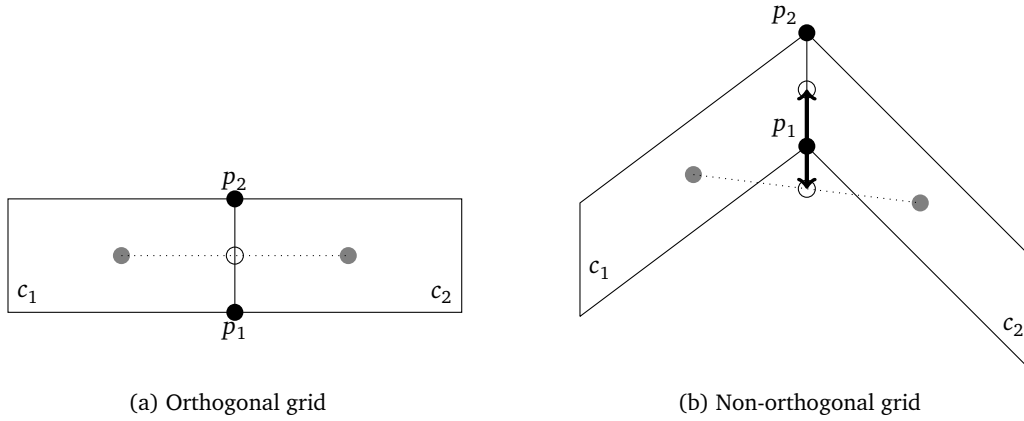


Figure 2.3: Skewness measurements on two-cell grids. Cell centres are represented by grey circles, and face vertices by filled black circles. The face centre and the intercept with the dotted line that joins the cell centres are denoted by open circles. In the orthogonal grid (a), skewness is zero. In the non-orthogonal grid (b), the skewness is measured by the double-ended arrow.

face f , and the intercept of a line connecting the centres of c_1 and c_2 with the line passing through points p_1 and p_2 (Moraes et al. 2013).

In an orthogonal grid, seen in figure 2.3a, the skewness is zero. Skewness increases when the grid becomes non-orthogonal, as shown in figure 2.3b. If high accuracy is required, a numerical scheme must account for this skewness when interpolating values at cell face.

2.7 Vertical staggering of variables

There are two commonly-used vertical stagarrings, the Lorenz grid (Lorenz 1960) and the Charney–Phillips grid (Charney and Phillips 1953), which offer different sets of computational and physical properties.

In both grids, horizontal velocities u and v , and density ρ , are stored at full levels, and the vertical velocity, w , is stored at half levels. The two grids differ in their placement of potential temperature, θ : on the Charney–Phillips grid it is stored at half levels, and at full levels on the Lorenz grid. These arrangements of variables are summarised in figure 2.4. The placement of thermodynamic variables leads to different representations of hydrostatic balance in simulations of flows involving buoyancy.

The Charney–Phillips grid was originally developed for a quasi-geostrophic model using sigma coordinates. Arakawa and Moorthi (1988) found that advection of quasi-geostrophic potential vorticity is conserved by this grid staggering, and it requires less interpolation of variables than the Lorenz grid (Holdaway et al. 2013a).

The Lorenz grid has a number of desirable properties: it conserves total energy, the mean potential temperature, and variance of potential temperature assuming no diabatic processes or friction (Arakawa and Konor 1996). However, it is known that a computational mode exists on the Lorenz grid which can create a zig-zag in the vertical distribution of potential temperature (Arakawa and Moorthi 1988;

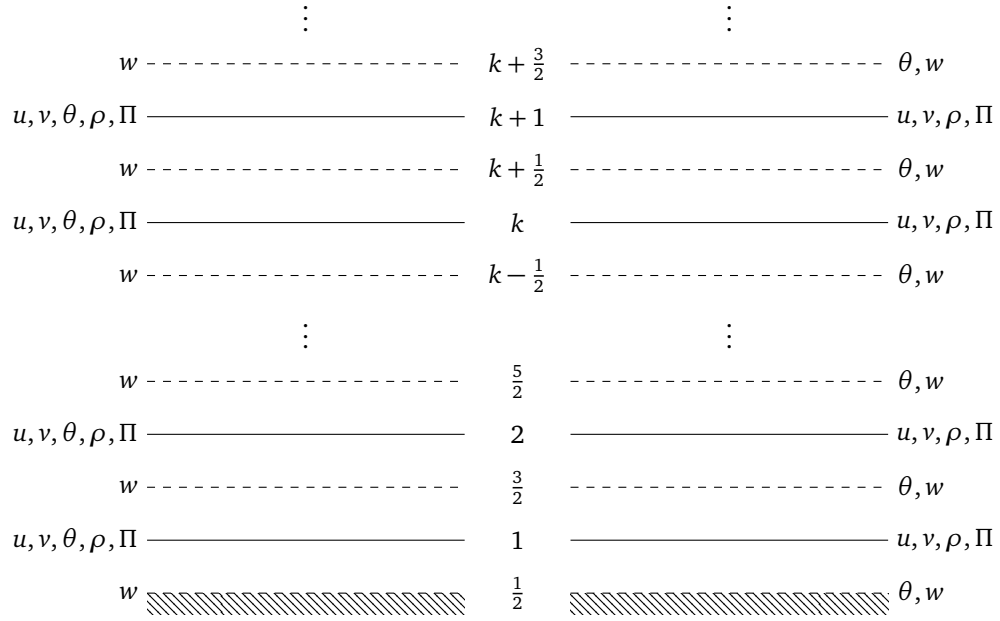


Figure 2.4: Lorenz (left) and Charney–Phillips (right) vertical staggering of variables. Solid lines represent full levels, dashed lines represent half levels. Adapted from Holdaway et al. (2013a).

Arakawa and Konor 1996; Holdaway et al. 2013b). This can be explained by considering the vertical momentum equation (Holdaway et al. 2013a)

$$\frac{\partial w}{\partial t} + \mathbf{u} \cdot \nabla w = -g - c_p \theta \frac{\partial \Pi}{\partial z} \quad (2.19)$$

where \mathbf{u} is the velocity field, g is the gravitational acceleration, c_p is the heat capacity of dry air at constant pressure, $\theta = T (p_0/p)^\kappa$ is the potential temperature, T is the temperature, $\Pi = (p/p_0)^\kappa$ is the Exner function of pressure, p is the pressure, p_0 is a reference pressure, $\kappa = R/c_p$, and R is the specific gas constant of dry air.

In a discretisation of this equation, to calculate $w_{k+\frac{1}{2}}$, $\theta_{k+\frac{1}{2}}$ may be interpolated using an arithmetic mean of the adjacent values θ_k and θ_{k+1} . As shown in figure 2.5, a grid-scale vertical wave in potential temperature would not be visible by the model (Holdaway et al. 2013a). Despite the oscillations, hydrostatic balance is satisfied and w is everywhere zero.

The computational mode can affect the physical mode, causing spurious interactions with condensation processes (Arakawa and Konor 1996) and the spurious generation of baroclinic instability and increased gravity wave activity (Arakawa and Moorthi 1988; Cullen et al. 1997). The computational mode is not present on the Charney–Phillips grid.

2.8 Gravity waves

When an air parcel is forced to rise over a mountain, it experiences a restoring buoyancy force which can create waves that propagate away from the mountain. These are known as gravity waves, mountain

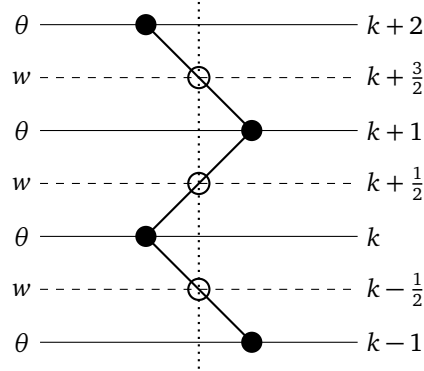


Figure 2.5: Interpolation of potential temperature on a Lorenz grid. Solid circles denote values of θ stored at full levels and the solid line shows the potential temperature profile. Open circles denote θ values interpolated onto half levels and the dotted line represents the interpolated profile. Magnitude of θ increases to the right.

waves, or lee waves.

Gravity waves play an important role in mesoscale weather. The waves can trigger convection by propagating through areas of weak stability, they cause clear-air turbulence that affects aircraft (Ray 1986), and can produce very strong downslope winds on the lee slope of the mountain (Holton et al. 2003).

In this section, we briefly present the theory of linear waves and demonstrate their effect on wind and temperature. In section 4.4, we relate this theory to the results of a two dimensional experiment in which gravity waves are induced by flow over a wave-shaped mountain range.

Two dimensional waves in the $x - z$ plane are characterised by their frequency, ω , amplitude A , and their horizontal and vertical wavenumbers, k and m . In flow over a mountain, the horizontal wavenumber is often related to the spacing between mountain ridges. By starting with the Boussinesq approximation of the Navier-Stokes equations we can derive the dispersion relation (Lynch and Cassano 2006)

$$\left(\frac{\partial}{\partial t} + \bar{u} \frac{\partial}{\partial x}\right)^2 \left(\frac{\partial^2 w'}{\partial x^2} + \frac{\partial^2 w'}{\partial z^2}\right) + N^2 \frac{\partial^2 w'}{\partial x^2} = 0 \quad (2.20)$$

where \bar{u} is the mean horizontal wind and w' is the vertical velocity anomaly. This can be solved by assuming a wave-like solution

$$w' = A \cos(kx + mz - \omega t) \quad (2.21)$$

thus giving the dispersion relation

$$(\omega - \bar{u}k)^2 (k^2 + m^2) - N^2 k^2 = 0 \quad (2.22)$$

The potential temperature anomaly θ' is a function of background stability $\partial \bar{\theta} / \partial z$ and is 90° out of phase with w' , given by (Lynch and Cassano 2006)

$$\theta' = \frac{A}{\omega} \frac{d\bar{\theta}}{dz} \sin \phi \quad (2.23)$$

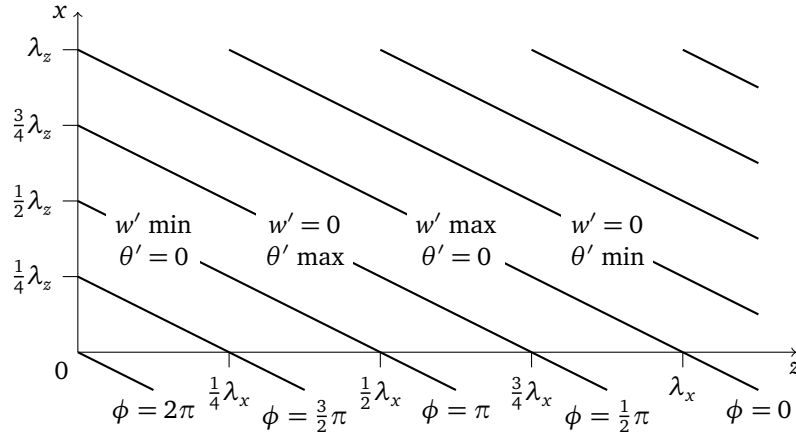


Figure 2.6: Phase relationship between vertical velocity anomalies w' and potential temperature anomalies θ' . Adapted from Lynch and Cassano (2006).

where the phase ϕ is

$$\phi = kx + mz - \omega t \quad (2.24)$$

Using equations 2.21, 2.23 and 2.24 we can plot the phase relationships between w' and θ' , shown in figure 2.6.

Next, we impose a lower boundary condition to simulate flow over an infinite, wave-shaped terrain and find that two types of stationary wave exist. Consider a surface, the height of which is defined by $h(x)$, such that

$$h(x) = h_0 \cos(kx) \quad (2.25)$$

The flow at any point at the surface must be parallel to that surface (that is, a no normal flow boundary condition)

$$w(x, 0) = \frac{dh}{dt} \quad (2.26)$$

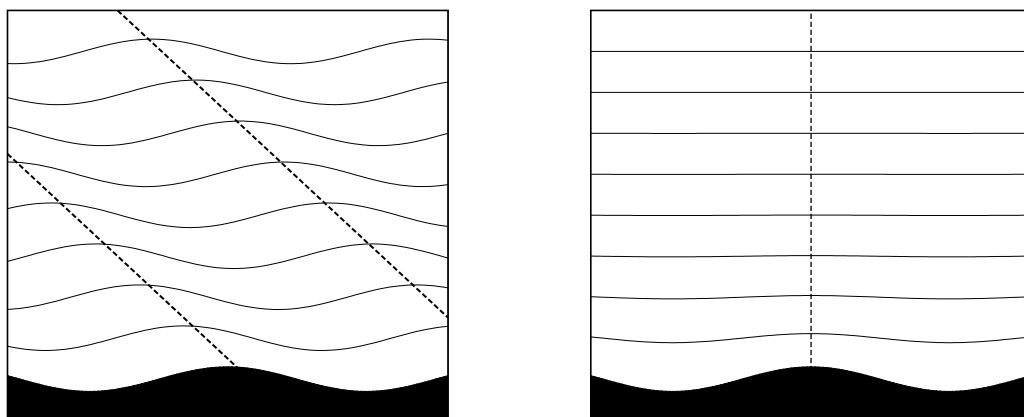
$$= \bar{u} \frac{\partial h}{\partial x} \quad (2.27)$$

$$= -\bar{u} k h_0 \sin(kx) \quad (2.28)$$

Assuming a stationary wave in the form $w'(x, z) = -\bar{u} k h_0 \sin(kx + mz)$, and noting that $\partial/\partial t = 0$ and $\omega = 0$, we find that the dispersion relation given by equation 2.22 has the solution (Lynch and Cassano 2006)

$$m = \sqrt{\frac{N^2}{\bar{u}^2} - k^2} \quad (2.29)$$

which also satisfies the boundary condition given by equation 2.28. The solution is presented in figure 2.7a which shows the vertically propagating wave.



(a) Vertically propagating gravity wave

(b) Evanescent wave showing rapid decay in height and no vertical propagation

Figure 2.7: Example vertical cross sections of streamlines for stationary gravity waves over infinite sinusoidal terrain. Thick dashed lines denote lines of constant phase. Adapted from Lynch and Cassano (2006).

We see from equation 2.29 that, for m to have a real solution, $|\bar{u}k| < N$. This constraint cannot be satisfied when the wind is too strong, stability is too weak, or the spacing of mountain ridges is too narrow (that is, k is too large). In this case, the dispersion relation is instead satisfied by the solution (Lynch and Cassano 2006)

$$w' = -\bar{u}kh_0 e^{-mz} \sin(kx) \quad (2.30)$$

As shown in figure 2.7b, in this solution, waves decay with height and there is no vertical propagation. These are often called evanescent waves.

3 Methodology

Here, we describe the construction of BTF and SLEVE terrain following grids and a cut cell style grid. A finite volume model of the fully-compressible Euler equations from Weller and Shahrokhi (2014) is summarised. In the next chapter, five tests are presented in which this model is run on the terrain following and cut cell grids. Finally, we give details of energy measures and the Courant–Friedrich–Lewy criterion, which constraints the model timestep. These metrics are used to evaluate model performance in chapter 4.

3.1 Grid construction

A combination of standard and custom OpenFOAM utilities were used to create three grids: BTF, SLEVE, and a cut cell style grid. OpenFOAM grids comprise a set of cells connected by shared faces. A face is composed from a list of points that form the face vertices. OpenFOAM uses a three dimensional Cartesian coordinate system. Since all tests presented here are two dimensional $x - z$ plane, empty boundary conditions are used on the front and back faces to ensure that no solutions are required in the y direction.

Two dimensional, regular Cartesian grids were created using the OpenFOAM utility, `blockMesh`. A custom utility was used to modify these orthogonal grids by adjusting the height of points to create terrain following grids.

Most implementations of terrain following layers use a coordinate system that makes the domain rectangular, but introduces metric terms into the equations of motion (more detail was presented in section 2.1). Instead, the model presented here uses Cartesian coordinates and unstructured grids. By doing so, results from the same model can be compared between terrain following and cut cell grids without modifying the equation set or discretisation.

At the time of writing, there is no OpenFOAM utility to generate cut cell grids¹. Instead, the OpenFOAM utility `snappyHexMesh` was used to create a grid that approximates the cut cell method. First, a custom utility was used to move points beneath the surface up to the surface creating small cells near mountain peaks. Second, a description of the surface was taken from any of the terrain following

¹An enhancement request was filed in 2013 to add support for Cartesian cut cells to OpenFOAM, see <http://www.openfoam.org/mantisbt/view.php?id=1083>

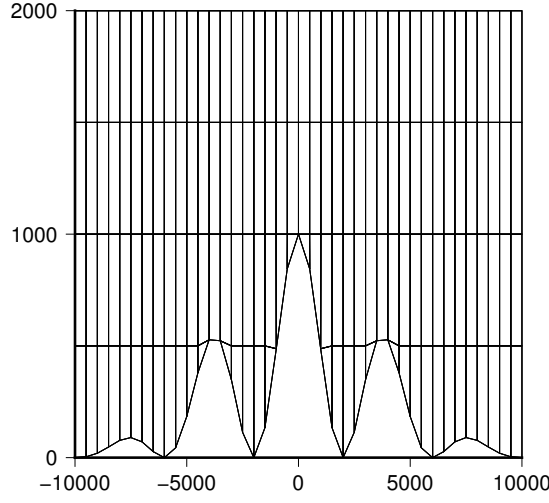


Figure 3.1: A ‘SnapCol’ grid, 20 km wide and 2 km high, created by intersecting the terrain surface with a regular grid as described in section 3.1. Note that, unlike a true cut cell grid, some small cells have faces at $z = 500$ m that are not entirely horizontal.

grids and `snappyHexMesh` was used to intersect the surface with the grid. The tool removes cells whose centres are below the surface. An example of the resulting grid is shown in figure 3.1.

There are some issues with grid construction which mean that this is not strictly a cut cell grid. First, when `snappyHexMesh` moves points along the surface according to its heuristics, some points are moved horizontally. Second, the utility does not create new points necessary for pentagonal cells, such as those seen in figure 2.2c. It has not been possible to correct these issues for this project. Henceforth, this grid is referred to as the ‘SnapCol’ grid.

3.2 Discretisation of Euler equations

The fully-compressible Euler equations used in the resting atmosphere test (section 4.3) and gravity waves test (section 4.4) are specified as

$$\text{Momentum} \quad \frac{\partial \rho \mathbf{u}}{\partial t} + \nabla \cdot \rho \mathbf{u} \mathbf{u} = \rho \mathbf{g} - c_p \rho \theta \nabla \Pi \quad (3.1a)$$

$$\text{Continuity} \quad \frac{\partial \rho}{\partial t} + \nabla \cdot \rho \mathbf{u} = 0 \quad (3.1b)$$

$$\text{Potential temperature} \quad \frac{\partial \rho \theta}{\partial t} + \nabla \cdot \rho \mathbf{u} \theta = 0 \quad (3.1c)$$

$$\text{Equation of state} \quad \Pi^{(1-\kappa/\kappa)} = \frac{R \rho \theta}{p_0} \quad (3.1d)$$

where ρ is the density and \mathbf{g} is gravitational acceleration. Other variables are as defined in section 2.7.

Here, we outline the placement of prognostic variables, pressure gradient discretisation, and the advection scheme. Further details of the discretisation are given by Weller and Shahrokhi (2014).

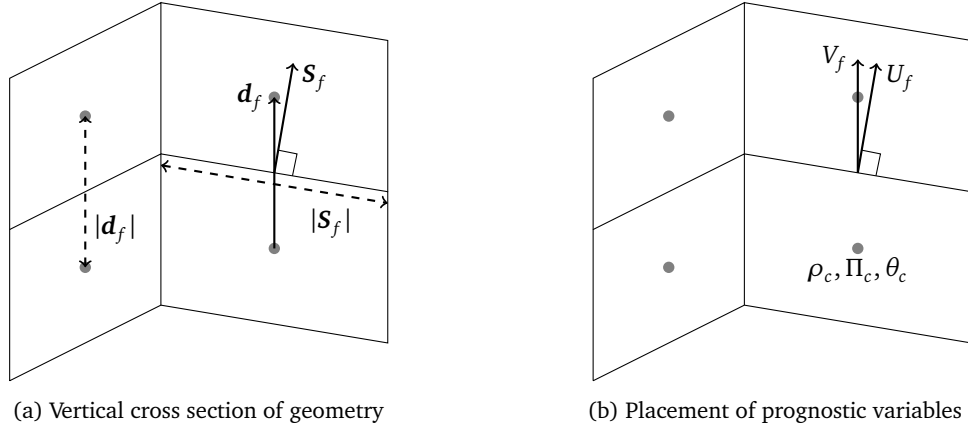


Figure 3.2: Geometric placement of prognostic variables in two dimensions. Adapted from Weller and Shahrokhi (2014).

Because the model operates on an unstructured grid, it does not use the horizontal and vertical pressure gradients commonly employed by structured grid models. Instead, the Exner gradient at a face f in the direction between cell centres, $\nabla_d \Pi$, is calculated from the Exner value of the two cells who share the face (Weller and Shahrokhi 2014)

$$\nabla_d \Pi = \frac{1}{|\mathbf{d}_f|} \sum_{c \in f} -n_f \Pi_c \quad (3.2)$$

where \mathbf{d}_f is the vector between the centres of the two cells who share the face f , and n_f corrects for the face orientation so that

$$n_f = \begin{cases} 1 & \text{if } \mathbf{S}_f \text{ points away from the cell} \\ -1 & \text{if } \mathbf{S}_f \text{ points toward the cell} \end{cases} \quad (3.3)$$

As discussed in section 2.6, equation 3.2 is second-order accurate where the grid is uniform, and first-order accurate elsewhere.

To solve the continuity equation (equation 3.1b), in section 2.5 we found that we must calculate the flux across all cell faces (see equation 2.18). To do this, we first find the mass flux component V_f in the direction between cell centres such that

$$V_f = \rho \mathbf{u} \cdot \mathbf{d}_f \quad (3.4)$$

Second, we use the H operator given in Weller and Shahrokhi (2014) to find the mass flux normal to the surface, U_f , that is

$$U = HV \quad (3.5)$$

where $U_f = \rho \mathbf{u} \cdot \mathbf{S}_f$, and \mathbf{S}_f is normal to the face f having a magnitude equal to the face area. Thuburn and Cotter (2012) recommend the use of V instead of U as the prognostic variable to obtain mimetic

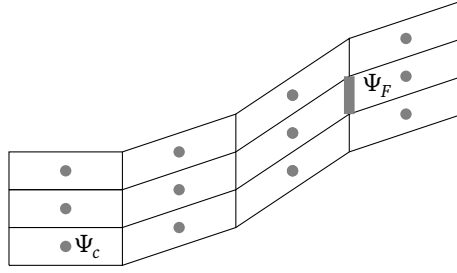


Figure 3.3: Two-dimensional cubic upwind stencil used in advecting momentum and potential temperature. A face value Ψ_F is interpolated from cell values, Ψ_c , denoted by grey dots. Adapted from Weller and Shahrokhi (2014).

properties including a curl-free pressure gradient. The geometry just described is summarised in figure 3.2.

As shown in figure 3.2b, the discretisation uses a Lorenz vertical staggering, as described in section 2.7, with θ stored at the cell centre.

While the pressure gradient is calculated in the direction of \mathbf{d} , continuity must be calculated in the direction of \mathbf{s} in order to find the mass flux through the faces. The H operator, which performs this transformation, is a source of numerical error. This is analogous to the errors introduced in calculating the horizontal pressure gradient, as described in section 2.2.

Momentum and potential temperature are advected using an upwind-biased cubic interpolation. A multi-dimensional cubic function is used whose coefficients are found using a least-squares fit with cell data in the stencil. These coefficients are used to weight the cell values within the stencil, and the weighted sum is used to calculate Ψ_F . A two-dimensional stencil is shown in figure 3.3.

3.3 Energy measures

Energy conservation is desirable in the discretisation of the Euler equations. In the resting atmosphere test detailed in section 4.3, energy is conserved in the analytic solution, but not in all numerical approximations. The normalised energy change ΔE at time t is found by comparing with the initial energy measure, hence

$$\Delta E(t) = \frac{E(t) - E(t = 0s)}{E(t = 0s)} \quad (3.6)$$

Three energy measures are considered. The volume integral of some field φ is the volume-weighted sum given by

$$\int_{\mathcal{V}} \varphi \, d\mathcal{V} = \frac{\sum_c \varphi_c \mathcal{V}_c}{\sum_c \mathcal{V}_c} \quad (3.7)$$

First, kinetic energy E_K is calculated as (Thuburn et al. 2014)

$$E_K(t) = \int_{\mathcal{V}} \frac{1}{4} \sum_{f \in c} \frac{UV}{\rho \mathcal{V}_c} \, d\mathcal{V} \quad (3.8)$$

Second, potential energy E_p is

$$E_p(t) = - \int_{\mathcal{V}} \rho \mathbf{g} \cdot \mathbf{x}_c \, d\mathcal{V} \quad (3.9)$$

where \mathbf{x}_c is the position vector of the centre of cell c . Third, the internal energy E_I is (Curry and Webster 1998)

$$E_I(t) = \int_{\mathcal{V}} \rho T c_v \, d\mathcal{V} \quad (3.10)$$

$$= \int_{\mathcal{V}} \rho T \left(\frac{p_0}{p} \frac{p}{p_0} \right)^{R/c_p} c_v \, d\mathcal{V} \quad (3.11)$$

$$= \int_{\mathcal{V}} \rho \theta \Pi c_v \, d\mathcal{V} \quad (3.12)$$

where c_v the heat capacity of dry air at constant volume, assuming an perfect gas with constant c_v .

3.4 Courant–Friedrichs–Lewy criterion

The Courant–Friedrichs–Lewy (CFL) criterion is a necessary condition for numerical stability (though it is not always, by itself, a sufficient condition). For an explicit advection scheme, it constrains the timestep as a function of wind speed and cell volume. This is especially relevant for the small cells produced by the piecewise linear shaving technique described in section 2.4.

The CFL criterion states that the numerical domain of dependence must contain the true domain of dependence for the scheme to be convergent (LeVeque 2002).

On a two-dimensional unstructured grid, the Courant number for cell c is (Weller and Shahrokhii 2014)

$$\text{Co}_c = \frac{\Delta t}{2\mathcal{V}_c} \sum_{f \in c} \mathbf{u} \cdot \mathbf{S}_f \quad (3.13)$$

so that the CFL criterion is $\text{Co}_c \leq 1 \, \forall c$.

4 Results

A variety of two-dimensional test cases were performed over idealised terrain, solving the linear advection equation and the compressible Euler equations. The tests are designed to expose errors associated with both terrain following and cut cell grids. For each test, results on the BTF, SLEVE, and the cut cell style ‘SnapCol’ grid are compared. Tests that use terrain following velocity fields omit results for the SLEVE grid.

4.1 Horizontal tracer advection

Following Schär et al. (2002), a tracer is transported above orography by solving the advection equation for a prescribed horizontal wind. This challenges the accuracy of the advection scheme in the presence of grid distortions. The wind profile, terrain profile and initial tracer field are shown in Figure 4.1.

Specification

The domain is 300 km wide and 25 km high. The terrain is wave-shaped, specified by the surface height h such that

$$h(x) = \cos^2\left(\frac{\pi x}{\lambda}\right) h^* \quad (4.1a)$$

where

$$h^*(x) = \begin{cases} h_0 \cos^2\left(\frac{\pi x}{2a}\right) & \text{if } |x| < a \\ 0 & \text{otherwise} \end{cases} \quad (4.1b)$$

where $a = 25$ km is the mountain half-width, $h_0 = 3$ km is the maximum mountain height, and $\lambda = 8$ km is the wavelength. On the SLEVE grid, the large-scale component h_1 , as described in section 2.3, is given by

$$h_1(x) = \frac{1}{2} h^*(x) \quad (4.2)$$

and $s_1 = 15$ km is the large scale height, and $s_2 = 2.5$ km is the small scale height. The optimisation of SLEVE by Leuenberger et al. (2010) is not used, so the exponent $n = 1$. For comparison, the same tests were performed with no orography, such that $h = 0$ km everywhere.

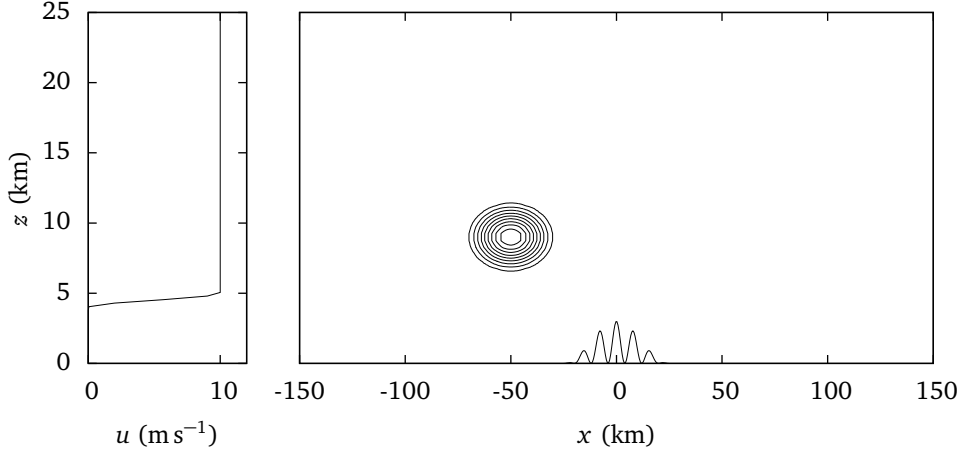


Figure 4.1: Vertical cross section of the two-dimensional advection test showing the horizontal wind profile, surface terrain profile and tracer field at $t = 0$ s on a $300 \text{ km} \times 25 \text{ km}$ domain. Adapted from Schär et al. (2002).

The wind is entirely horizontal and is prescribed as

$$u(z) = u_0 \begin{cases} 1 & \text{if } z \geq z_2 \\ \sin^2\left(\frac{\pi}{2} \frac{z-z_1}{z_2-z_1}\right) & \text{if } z_1 < z < z_2 \\ 0 & \text{otherwise} \end{cases} \quad (4.3)$$

where $u_0 = 10 \text{ m s}^{-1}$, $z_1 = 4 \text{ km}$ and $z_2 = 5 \text{ km}$. This results in a constant wind aloft, and zero flow at 4 km and below. A tracer φ is positioned upstream above the height of the terrain. It has the shape

$$\varphi(x, z) = \varphi_0 \begin{cases} \cos^2\left(\frac{\pi r}{2}\right) & \text{if } r \leq 1 \\ 0 & \text{otherwise} \end{cases} \quad (4.4)$$

having radius r given by

$$r = \sqrt{\left(\frac{x-x_0}{A_x}\right)^2 + \left(\frac{z-z_0}{A_z}\right)^2} \quad (4.5)$$

where $A_x = 25 \text{ km}$, $A_z = 3 \text{ km}$ are the horizontal and vertical half-widths respectively, and $\varphi_0 = 1$ is the maximum magnitude of the anomaly. At $t = 0$ s, the anomaly is centred at $(x_0, z_0) = (-50 \text{ km}, 9 \text{ km})$ so that the anomaly is upwind of the mountain and well above the maximum terrain height of 3 km. Analytic solutions can be found by adjusting the anomaly centre such that $x_0 = ut$.

Discretisation

The OpenFOAM solver `scalarTransportFoam` was used to implicitly solve the advection equation in flux form

$$\frac{\partial \varphi}{\partial t} + \nabla \cdot (\mathbf{u} \varphi) = 0 \quad (4.6)$$

The solver uses a velocity field with values defined at cell centres, and linearly interpolates onto cell faces during the model initialisation phase.

The time derivative is solved implicitly using a backward-in-time, second order accurate scheme. At time level n , the time derivative, $\partial \varphi / \partial t$, is (OpenCFD Foundation 2014a)

$$\frac{\partial}{\partial t} \int_{\mathcal{V}} \varphi \, d\mathcal{V} = \frac{3(\varphi \mathcal{V})^{(n)} - 4(\varphi \mathcal{V})^{(n-1)} + (\varphi \mathcal{V})^{(n-2)}}{2\Delta t} \quad (4.7)$$

Spatial discretisation follows the finite volume method described in section 2.5, using the upwind-biased advection scheme described in section 3.2. The domain is discretised onto a grid having 300×50 cells such that $\Delta x = 1$ km and $\Delta z^* = 500$ m. Unlike Schär et al. (2002) who use periodic lateral boundaries, we use a fixed value of 0 at the inlet boundary and zero gradient boundaries elsewhere. Tests are integrated forward in time for 10 000 s with a timestep $\Delta t = 25$ s.

Diagnostics

Results of advection are evaluated using five metrics. First, tracer contours are plotted to visualise the extent to which tracer shape and magnitude are preserved. Second, tracer error contours are found by subtracting the analytic solution from the numerical solution. Both sets of contours enable results to be compared with those from Schär et al. (2002). Third, preservation of tracer magnitude is quantified by finding the minimum and maximum tracer values at the end of the simulation. Fourth, divergence of the discrete velocity fields is calculated for comparison with plots of tracer magnitude.

Finally, error norms are calculated at $t = 10\,000$ s by comparing with the analytic solution. The ℓ^2 error norm is defined as

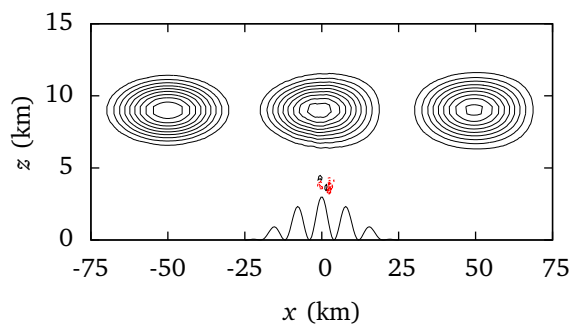
$$\ell^2 = \sqrt{\frac{\sum_c (\varphi - \varphi_T)^2 \mathcal{V}_c}{\sum_c (\varphi_T^2 \mathcal{V}_c)}} \quad (4.8)$$

where φ is the numerical tracer value, φ_T is the analytic value and \mathcal{V}_c is the cell volume. Because the test is two dimensional, the cell volume is equivalent to the cell area.

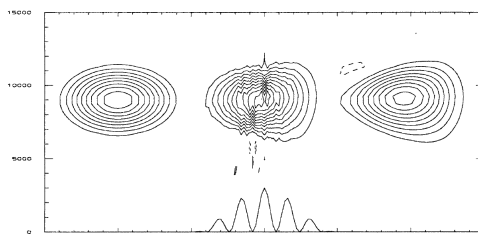
Analysis

Results of advection are presented in figure 4.2. On the BTF grid, the tracer suffers from distortion over the mountain and some artefacts just above the mountain remain as the tracer moves over it. Comparing figures 4.2a and 4.2b, we see that the tracer retains its shape far better than the result from Schär et al. (2002) that uses a second-order centred difference scheme. This is expected since the upwind-biased cubic scheme has a larger stencil and higher order accuracy. Comparing figures 4.3a and 4.3b we see that, unlike the results from Schär et al. (2002), errors on the BTF grid are confined to regions around the tracer and near the mountain peak.

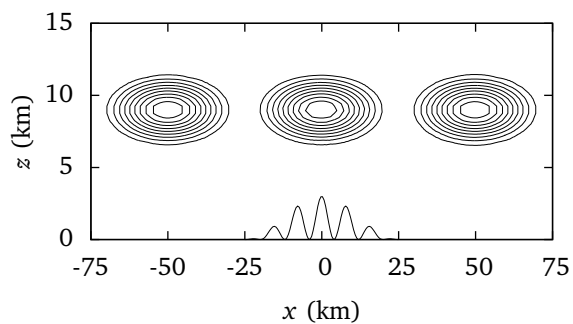
As seen in figure 4.2c, results on the SLEVE grid are much closer to the analytic solution on a regular grid (figure 4.2f). The tracer retains its shape throughout the simulation and does not suffer from any noticeable distortion. We find that accuracy is slightly better than the result from Schär et al.



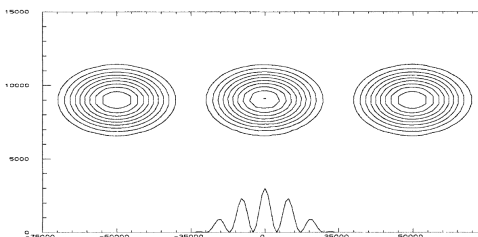
(a) BTf (negative contours at $t = 10000$ s near mountain peak shown as dashed red lines)



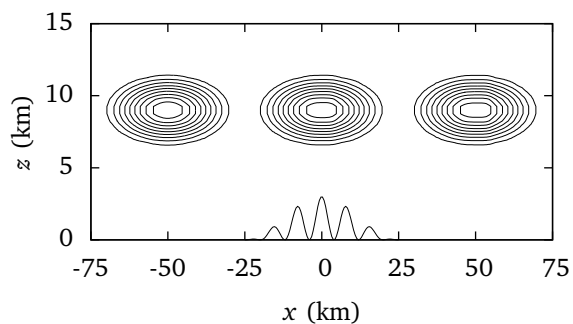
(b) BTf from Schär et al. (2002) (negative contours shown as dashed lines)



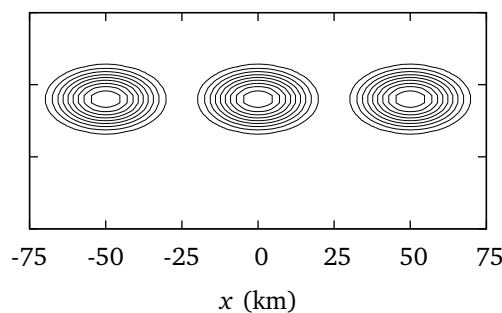
(c) SLEVE



(d) SLEVE from Schär et al. (2002)



(e) SnapCol grid



(f) Analytic solution on a regular grid

Figure 4.2: Horizontally advected tracer contours at $t = 0$ s, 5000 s and 10000 s. Figures (a), (c), and (e) use the upwind-biased scheme described in section 3.2. Figures (b) and (d) show the results of the second-order centred difference scheme from Schär et al. (2002). Contour intervals are every 0.1.

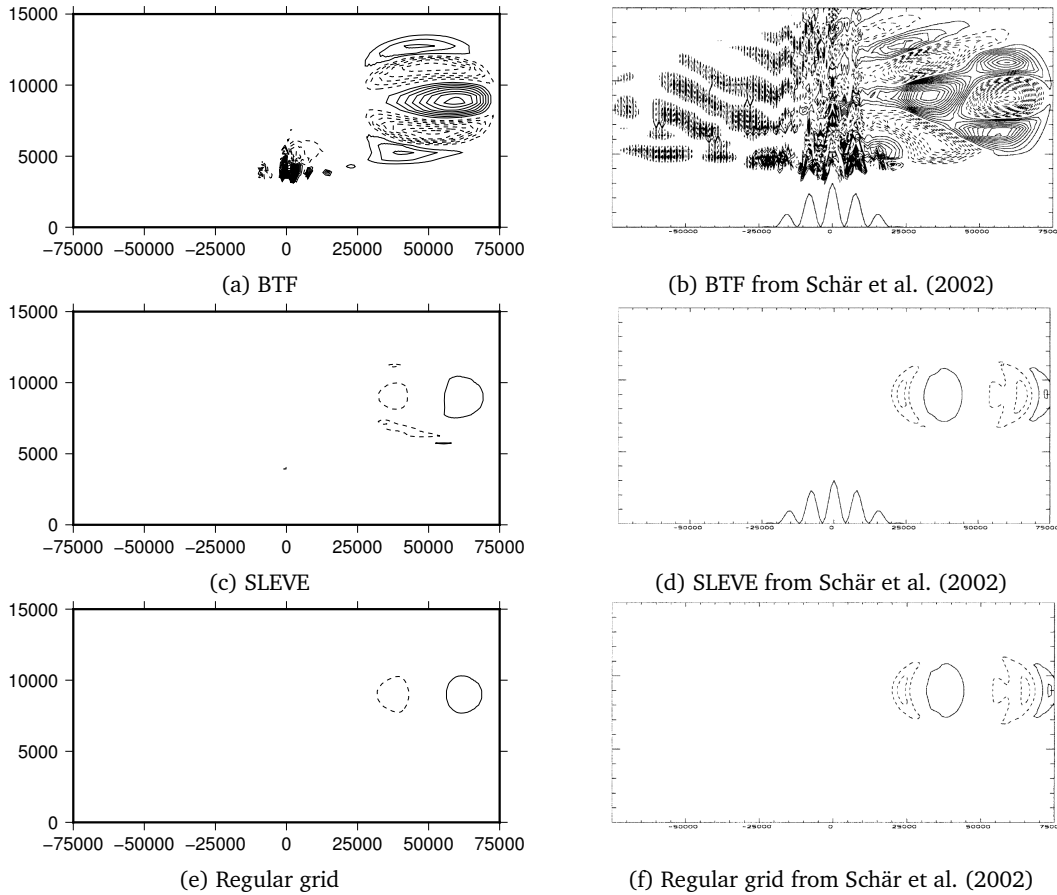


Figure 4.3: Errors in horizontal tracer advection at $t = 10000$ s. Figures (a), (c) and (e) use the upwind-biased scheme. Figures (b), (d) and (f) show the error of the second-order centred difference scheme from Schär et al. (2002). Contour intervals are every 0.01, with negative contours denoted by dashed lines.

(2002) (see figures 4.3c and 4.3d). Unlike Schär et al. (2002), a further improvement in accuracy is seen on a regular grid, as shown in figure 4.3e.

Since the SnapCol grid is entirely regular away from the surface, it is unsurprising that the results (shown in figure 4.2e) are the same as advection on a regular grid (not shown). This result agrees with that found by Good et al. (2014).

At $t = 0$ s, the tracer ranges between zero and one. Over time, new extrema are generated because the upwind-biased advection scheme is not monotonic. This is most evident on the BTF grid where the stationary artefacts above the mountain peak reach a minimum of -0.682 by the end of the simulation. The results of the second-order centred difference scheme of Schär et al. (2002) show significant negative tracer values as evidenced by the dashed contours in figure 4.2b. Minimum values remain close to zero on the SLEVE, SnapCol and regular grids. All grids show some decrease in maximum tracer magnitude and, once again, the decrease is most severe on the BTF grid. Results of tracer

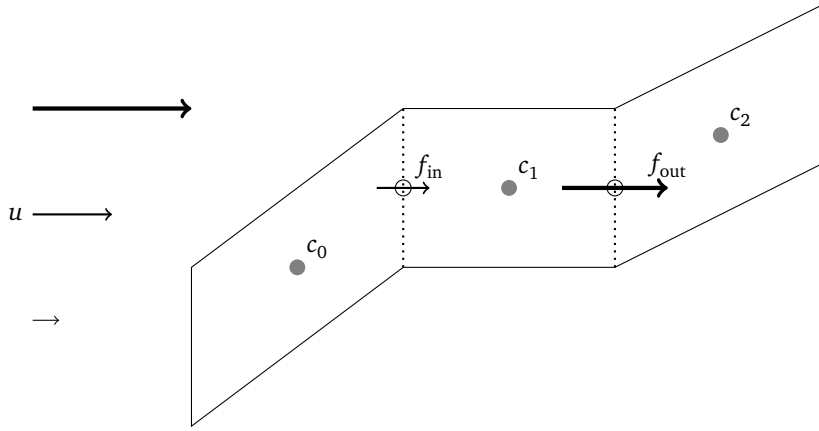


Figure 4.4: Flux through two faces, shown with dotted lines, in a rectangular cell in the region of vertical wind shear. Because the surrounding cells are non-orthogonal, interpolation onto cell faces results in a net outward flux which leads to a decrease in tracer magnitude. Cell centres are denoted by grey circles, face centres by open circles. Flux magnitude is indicated by arrow length and line thickness.

extrema on all grids are compared to the analytic solution in figure 4.9a and the values are given in table 4.1 on page 32.

Because the upwind-biased advection scheme is not monotonic, one source of new extrema is a divergent velocity field. Areas of convergence will increase tracer magnitude and areas of divergence will reduce it. Although the continuous velocity field in this test is non-divergent, this is not necessarily true of the discrete velocity field, especially where the grid is non-orthogonal.

Let us consider the fluxes in and out of the vertically-oriented faces, f_{in} and f_{out} , of a rectangular cell in the region of vertical wind shear such that its cell centre c_1 has a height $4 \text{ km} < z < 5 \text{ km}$. To its left is a cell whose centre, c_0 , is lower and to its right, a cell whose centre, c_2 , is higher. This situation is shown in figure 4.4.

During model initialisation, the solver interpolates velocities at cell centres onto cell faces, such that f_{in} is interpolated from c_0 and c_1 , and f_{out} is an interpolation of c_1 and c_2 . Remember that horizontal wind is increasing with height, $u(c_2) > u(c_1) > u(c_0)$, and so $f_{out} > f_{in}$. Therefore, there is a net divergence in the rectangular cell which leads to a decrease in tracer magnitude.

Divergence was calculated on the BTF, SLEVE and SnapCol grids using linear interpolation. Divergence is found between about 2 km and 6 km above the surface, which includes the region of vertical wind shear. As seen in figure 4.5c, divergence is most significant on the BTF grid, with magnitudes reaching $\sim 6 \times 10^{-3} \text{ s}^{-1}$. Divergence is also present on the SLEVE grid, shown in figure 4.5d, but magnitudes do not exceed $8 \times 10^{-4} \text{ s}^{-1}$. Compared to the BTF grid, the affected region is shallower on the SLEVE grid. The SnapCol grid is orthogonal except at the surface, where there is no flow and, hence, the velocity field on the SnapCol grid was found to be non-divergent.

Examining the tracer field at $t = 5000 \text{ s}$ on the BTF and SLEVE grids in figures 4.5a and 4.5b respectively, we see that tracer magnitude is most negative in cells that have the greatest divergence.

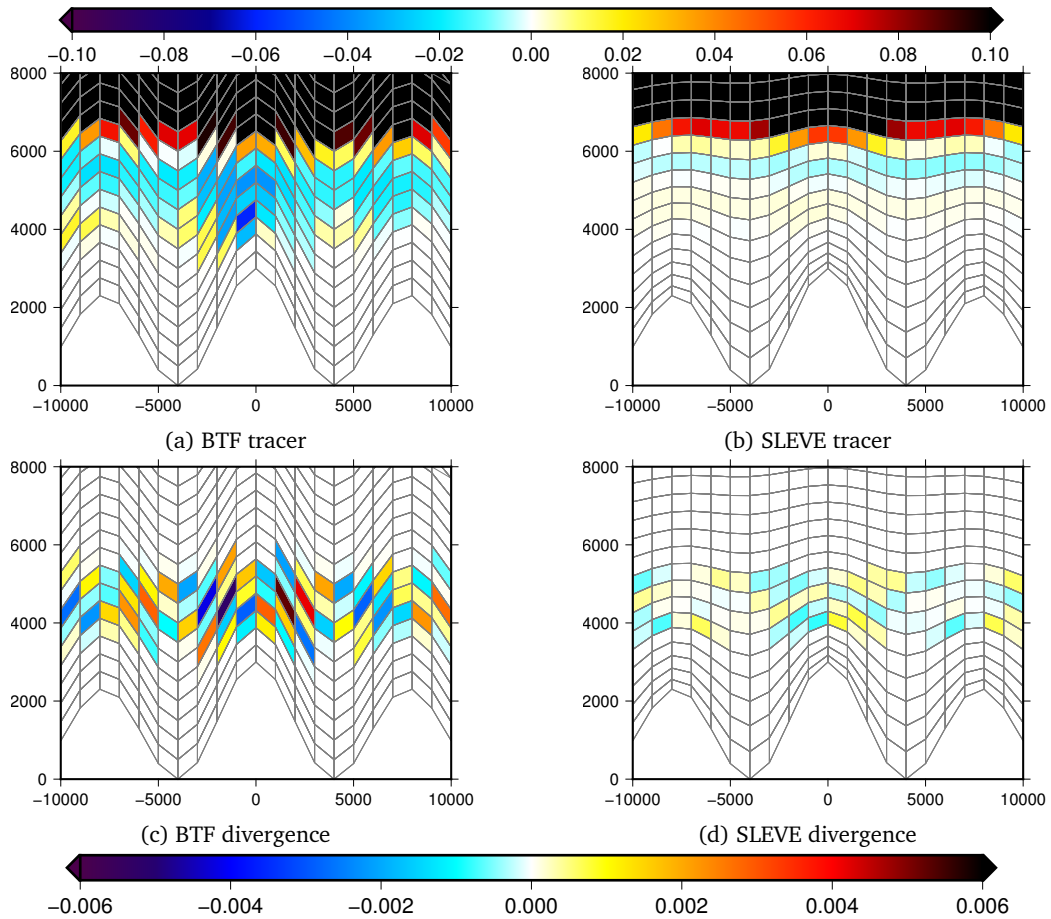


Figure 4.5: Tracer magnitude in the centremost 20 km and lowest 8 km at $t = 5000$ s on (a) the BTF grid, and (b) the SLEVE grid. The tracer colour scale, shown above the figures, is narrowed to reveal small magnitude errors. Divergence (s^{-1}) of the discrete velocity field is shown on (c) the BTF grid, and (d) the SLEVE grid. Divergence colour scale is shown below the figures. Results on the SnapCol grid are not shown since tracer errors above the mountain are minimal, and the discrete velocity field is entirely non-divergent.

Therefore, we conclude that divergence in the discrete velocity field is a cause of error in tracer magnitude.

The ℓ^2 error norms are summarised in table 4.1. Errors on the BTF grid are an order of magnitude greater than the three other grids tested. The cut cell grid offers only a small error reduction compared to the SLEVE grid. Even on the BTF grid, the upwind-biased advection scheme is far more tolerant of grid distortions than results of the fourth-order centred scheme from Schär et al. (2002) (not shown).

4.2 Terrain following tracer advection

In the horizontal advection test, results were more accurate when the flow was aligned with grid layers: on the cut cell grid results were accurate, but distortions in the BTF grid led to increased error. This terrain following advection test is designed to determine the nature of these errors by prescribing a velocity field that is aligned with the layers of the BTF grid. If errors are caused by skewness or grid non-uniformity (described in section 2.6), we expect least accuracy on terrain following grids since they are less orthogonal. However, if errors are caused by flow crossing grid layers, then results are expected to be less accurate on the SnapCol grid.

Specification

The spatial domain, mountain profile, initial tracer profile and discretisation are the same as those in the horizontal tracer advection test (section 4.1). The velocity field, however, is defined using a streamfunction Ψ so that the continuous velocity field is non-divergent. Unlike the horizontal advection test, flow extends from the top of the domain all the way to the ground. It is defined so that flow is everywhere tangential to BTF coordinate surfaces given by equation 2.10 such that

$$\Psi(x, z) = H \frac{z-h}{H-h} \quad (4.9)$$

The horizontal and vertical components of velocity, u and w are then given by

$$u = \frac{\partial \Psi}{\partial z}, \quad w = -\frac{\partial \Psi}{\partial x} \quad (4.10)$$

Hence, for the mountain profile given in equation 4.1 we find

$$u = \frac{H}{H-h}, \quad w = H \frac{\partial h}{\partial x} \frac{H-z}{(H-h)^2} \quad (4.11)$$

$$\frac{\partial h}{\partial x} = -h_0 \pi \left[\frac{1}{\lambda} \cos^2 \left(\frac{\pi x}{2a} \right) \sin \left(\frac{2\pi x}{\lambda} \right) + \frac{1}{2a} \cos^2 \left(\frac{\pi x}{\lambda} \right) \sin \left(\frac{\pi x}{a} \right) \right] \quad (4.12)$$

The resulting velocity field is shown in figure 4.6.

Analysis

The analytic solution at $t = 10000$ s is assumed to be the same as that for horizontal tracer advection given in section 4.1. Accuracy increases on the BTF grid compared to the horizontal tracer advection

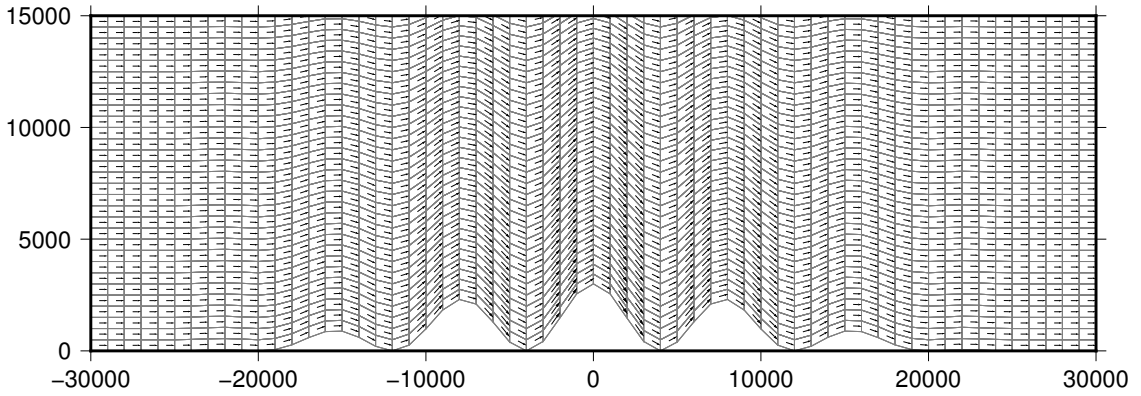


Figure 4.6: Terrain following velocity field with flow everywhere tangential to BTF coordinate surfaces. Outline of BTF grid shown in grey. Only the lowest 15 km of the central 60 km is shown. The entire domain is 300 km wide and 25 km high.

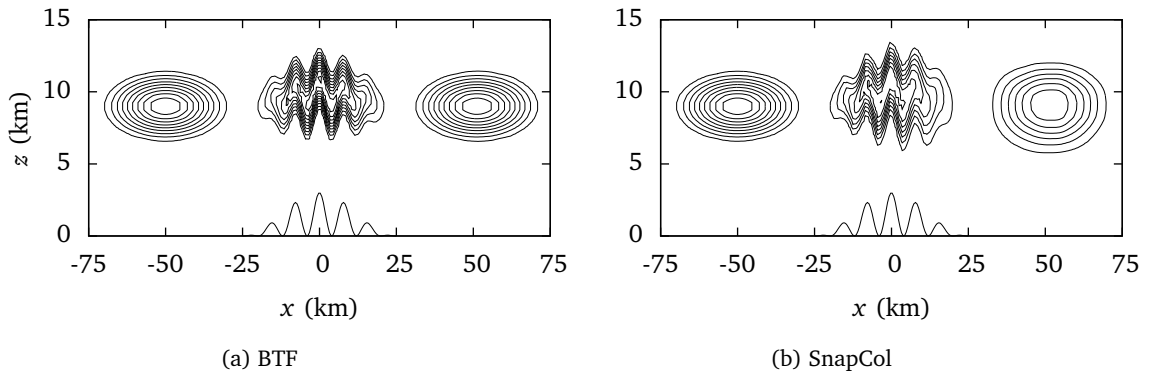


Figure 4.7: Advected tracer contours in a terrain following velocity field at $t = 0$ s, 5000 s and 10 000 s. Contour intervals are every 0.1.

test: artefacts above the mountain, as seen in figure 4.2a, are no longer present in figure 4.7a. This is confirmed by the absence of the large magnitude negative tracer, as shown in figure 4.9. The ℓ^2 error norm is reduced from 0.0106 to 0.00672. Despite the large distortions due to the oscillating velocity field above the mountain, tracer shape is preserved having cleared the mountain at $t = 10\,000$ s.

In contrast, the tracer suffers from significantly reduced accuracy on the SnapCol grid as evidenced by the fewer, wider contours in figure 4.7b. Accuracy on the SnapCol grid is lower than that for any other tracer advection. Tracer amplitude is reduced to 0.671 (see figure 4.9b). ℓ^2 error norms are compared with those for horizontal advection in table 4.1.

Divergence of the velocity fields was calculated on both grids in the same manner as the horizontal advection test. Divergence magnitudes, shown in figure 4.8, are negligible on both grids, except for cells immediately above the ground on the SnapCol grid. However, these cells do not affect the tracer which is transported well above the mountain peaks. Therefore, divergence has little effect on tracer magnitude in this test.

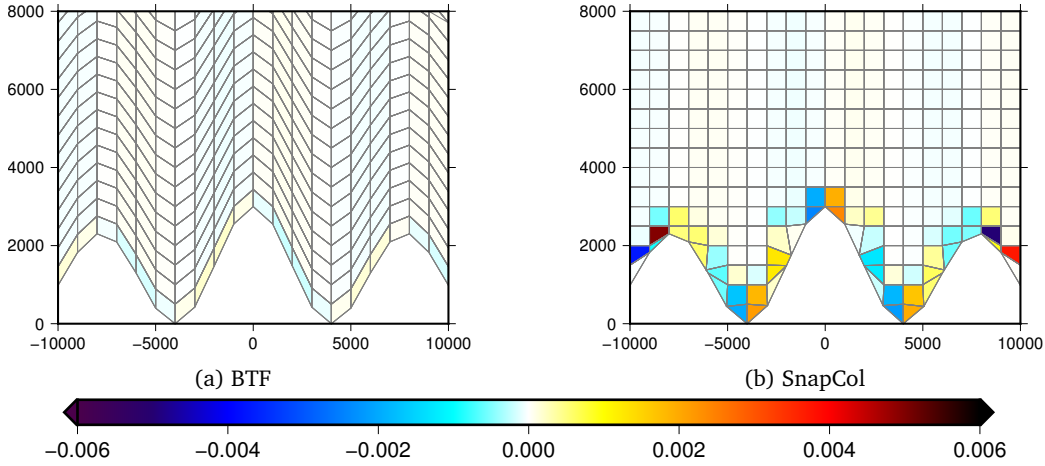


Figure 4.8: Divergence (s^{-1}) of the discrete velocity field in the centremost 20 km and lowest 8 km on (a) the BTF grid, and (b) the SnapCol grid.

	ℓ^2 error norm		Minimum		Maximum	
	Horizontal	TF	Horizontal	TF	Horizontal	TF
Analytic	0	0	0	0	1	1
BTF	0.0106	0.00672	-0.682	-0.0110	0.928	0.981
SLEVE	0.00163	—	-0.0106	—	0.981	—
SnapCol	0.00146	0.0229	-3.50×10^{-36}	-1.33×10^{-9}	0.963	0.671
Regular grid	0.00132	—	-0.00908	—	0.982	—

Table 4.1: ℓ^2 error norms, minimum and maximum tracer values for the horizontal and terrain following tracer advection tests at $t = 10000$ s. Horizontal tracer advection is discussed in section 4.1, terrain following advection in section 4.2, and only tested on BTF and SnapCol grids.

Given these results, we conclude that advection errors are mainly due to lack of flow alignment rather than skewness or grid non-uniformity.

4.3 Resting atmosphere

This two-dimensional test simulates a stratified atmosphere in hydrostatic balance, following the specification from Klemp (2011). Since there are no net forces, the analytic solution should remain at rest. An inversion layer causes nonlinear processes that further tax the model (Good et al. 2014). In their terrain following model, Klemp (2011) designed the test to challenge the accuracy in calculating the horizontal pressure gradient. Here, the test challenges the accuracy of the H operator which converts the velocity between cell centres, V , to the velocity normal to the face, U , where U and V are only equal where the grid is orthogonal.

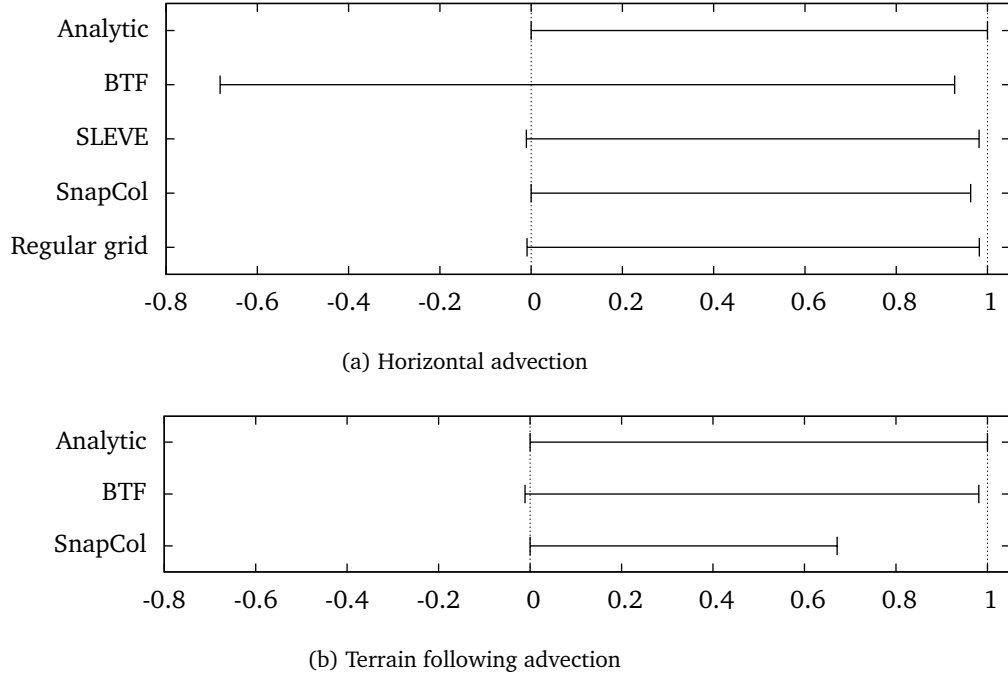


Figure 4.9: Comparison of minimum and maximum tracer values at $t = 10000$ s for horizontal and terrain following tracer advection tests. Initially, tracer magnitude ranges from zero to one.

Specification

Following Weller and Shahrokhi (2014), the domain is 20 km wide and 20 km high, which is narrower than Klemp (2011) in order to reduce simulation time. The wave-shaped mountain profile is taken from Schär et al. (2002) where the surface height h is given by

$$h(x) = h_0 \exp\left(-\left(\frac{x}{a}\right)^2\right) \cos^2\left(\frac{\pi x}{\lambda}\right) \quad (4.13)$$

where $a = 5$ km is the mountain half-width, $h_0 = 1$ km is the maximum mountain height and $\lambda = 4$ km is the wavelength. For the optimised SLEVE grid, the large-scale component h_1 , described in section 2.3, is specified as

$$h_1(x) = \frac{1}{2} h_0 \exp\left(-\left(\frac{x}{a}\right)^2\right) \quad (4.14)$$

and, following Leuenberger et al. 2010, $s_1 = 4$ km is the large scale height, $s_2 = 1$ km is the small scale height, and the optimal exponent value of $n = 1.35$ is used. Results are compared with the numerical solution with no orography.

The initial thermodynamic conditions have a surface temperature of $\theta_0 = 288$ K and constant stability with Brunt-Väisälä frequency $N = 0.01$ s⁻¹ everywhere, except for a more stable layer of $N = 0.02$ s⁻¹ between $2 \text{ km} \leq z \leq 3 \text{ km}$.

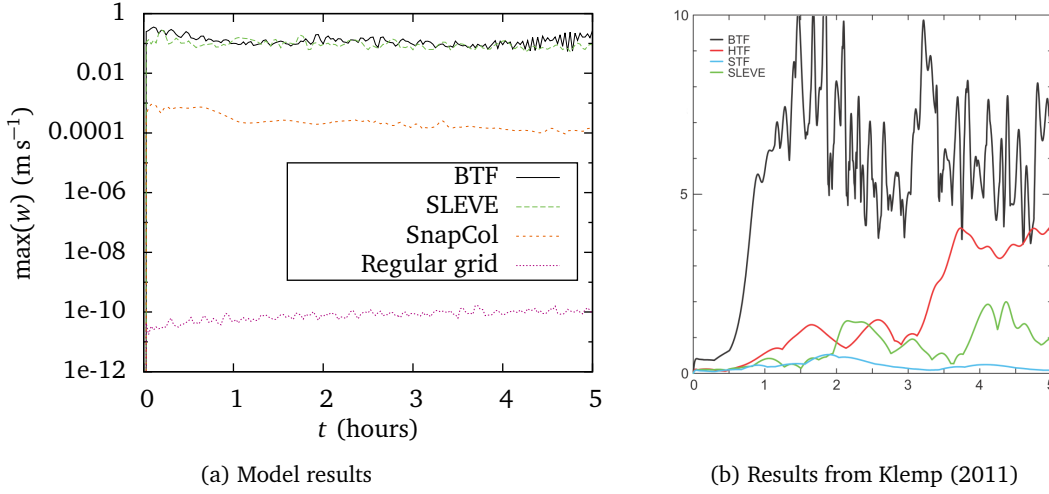


Figure 4.10: Maximum spurious vertical velocity w in the resting atmosphere test compared with results from Klemp (2011). Note that vertical scales differ.

Diagnostics

Two metrics were used to measure the model error. First, maximum vertical velocity is measured at each timestep. An analytic solution has no vertical velocity, w , since the atmosphere is at rest. However, numerical error in calculating the horizontal pressure gradient give rise to spurious vertical velocities which become more severe over steep terrain (Klemp 2011).

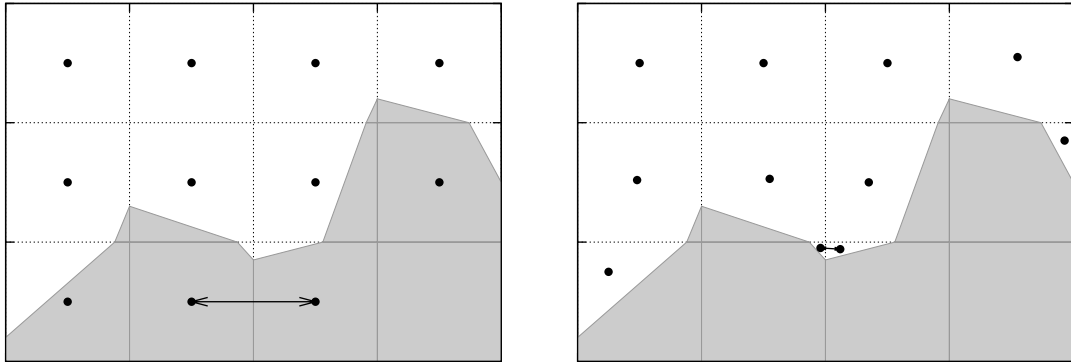
Second, normalised energy change ΔE is measured for each timestep as described in section 3.3. The total normalised energy change is the sum of normalised kinetic, potential, and internal energy changes. An analytic solution would conserve total energy such that $\Delta E(t) = 0 \forall t$. As discussed in Weller and Shahrokhi (2014), energy is not exactly conserved in the model presented because of damping by the advection scheme and inexact transfer between kinetic, internal and potential energy.

Discretisation

The simulation uses the discretisation of the fully-compressible Euler equations described in section 3.2. The domain is discretised on a grid having 40×40 cells such that $\Delta x = \Delta z = 0.5 \text{ km}$. All boundary conditions are no normal flow. The simulation is integrated forward by 5 hours with a timestep $\Delta t = 100 \text{ s}$. Unlike Klemp (2011), there is no eddy diffusion in the equation set.

Analysis

Test results for BTF, optimised SLEVE, and SnapCol grids are compared with results on a regular grid with no orography. On the BTF grid, spurious vertical velocity w reaches $\sim 0.35 \text{ m s}^{-1}$, which is significantly less than the velocities of $\sim 10 \text{ m s}^{-1}$ found by Klemp (2011) (see figure 4.10, note different vertical scales). An oscillation develops after 4 hours, the cause of which is not yet known. Unlike the



(a) Cell centres at centre of uncut cells leading to some cell centres below the ground

(b) Cell centres at centre of cut cells

Figure 4.11: Placement of cell centres on a two-dimensional cut cell grid. The model from Good et al. (2014) has some cell centres below the ground (S.-J. Lock 2014, personal communication). The arrows denote an estimated horizontal gradient between two adjacent cells of a scalar value stored at cell centres.

results from Klemp (2011), the optimised SLEVE grid does not significantly reduce w compared to BTF. Since the model and its initialisation are the same, results on the BTF and optimised SLEVE grids are also in agreement with Weller and Shahrokhi (2014).

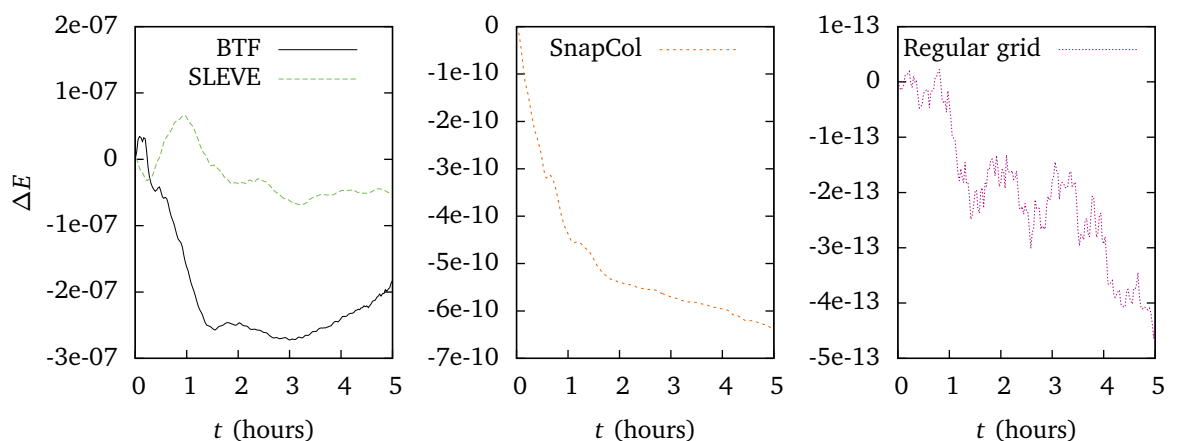
The SnapCol grid results in a significantly smaller maximum vertical velocity of less than $1 \times 10^{-3} \text{ m s}^{-1}$. The smallest error of $\sim 1 \times 10^{-10} \text{ m s}^{-1}$ is found on the regular grid. This error may be due to loss of precision when OpenFOAM loads the initial conditions, which are in discrete hydrostatic balance, but the source of the error is not certain.

Using a timestep of 1.01 s, Good et al. (2014) found the maximum vertical velocity in their cut cell model was $1 \times 10^{-12} \text{ m s}^{-1}$, which is better than any result from the experiments in this project. However, in that model, cell centres are in the centre of the uncut cell, resulting in the centre of some cut cells being below the ground, as shown in figure 4.11 (S.-J. Lock 2014, personal communication). This means that the grid is effectively regular when calculating horizontal and vertical gradients.

Examining normalised energy change, shown in figure 4.12a, we find that there is a net loss of energy on BTF and optimised SLEVE grids. However, there is a period of energy gain on the optimised SLEVE grid during the first two hours, and an upward trend in energy after 3 hours on the BTF grid. The cause of the energy gain is the subject of further work (see chapter 6).

Energy is better conserved on the SnapCol grid, the energy loss being more than two orders of magnitude smaller than the terrain following grids (figure 4.12b). This compares favourably with the best possible energy conservation for this model as found on a regular grid (figure 4.12c).

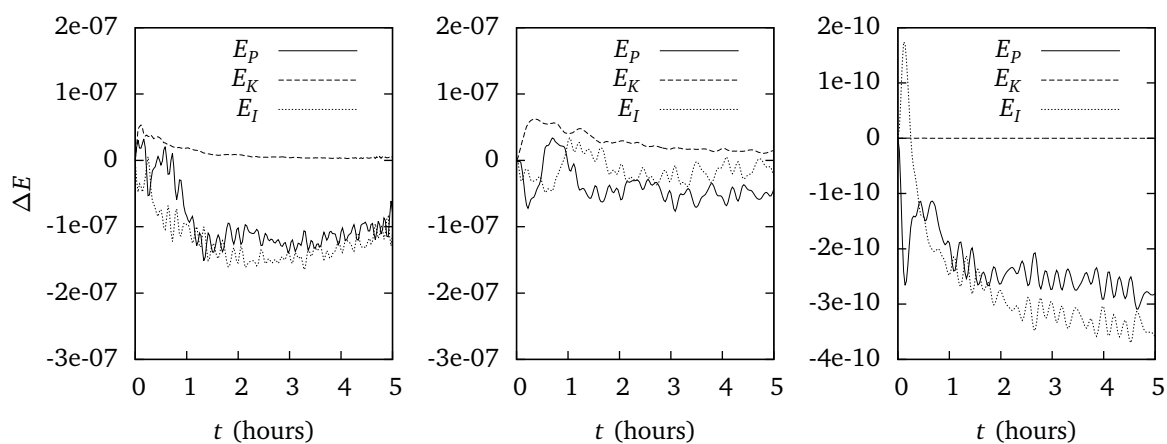
The spurious motion generated by horizontal pressure gradient errors leads to a positive change in kinetic energy, evident in figures 4.12d and 4.12e. Compared to both terrain following grids, internal and potential energy conservation is three orders of magnitude better on the SnapCol grid (4.12f). As



(a) Total normalised energy changes on terrain following grids

(b) As (a), but on the SnapCol grid

(c) As (a), but on a regular grid with no orography

(d) Kinetic (E_K), potential (E_P) and internal (E_I) normalised energy changes on BTF grid

(e) As (d), but on the optimised SLEVE grid

(f) As (d), but on the SnapCol grid. Note the different vertical scale from figures (d) and (e).

Figure 4.12: Comparison of normalised energy changes on BTF, optimised SLEVE and SnapCol grids for the resting atmosphere test.

noted by Weller and Shahrokhi (2014), the model converts between potential and internal energy on timescales of less than an hour. This can be seen by the mirroring between E_p and E_I plots, and we confirm that this local energy conservation property is present in all three grids (figures 4.12d, e and f).

We conclude that grid non-orthogonality is a significant cause of numerical error: spurious velocities in the presence of orography were smallest on the SnapCol grid, but spurious motions are far smaller than the results from Klemp (2011) even on the highly non-orthogonal BTF grid.

4.4 Gravity waves

Following Schär et al. (2002), uniform flow over an idealised two-dimensional mountain ridge induces gravity waves in a stable atmosphere. As described in section 2.8, large-scale waves propagate away from the surface and small-scale evanescent waves decay rapidly above the terrain.

Specification

Following Melvin et al. (2010), the domain is 300 km wide and 30 km high. The mountain profile has the same form as equation 4.13 but with a lower maximum height of $h_0 = 250$ m. As in the resting atmosphere test, $a = 5$ km is the mountain half-width and $\lambda = 4$ km is the wavelength. On the optimised SLEVE grid, $s_1 = 5$ km is the large scale height, $s_2 = 2$ km is the small scale height and the optimal exponent value $n = 1.35$ as in the previous test.

The initial thermodynamic conditions have a surface temperature of $\theta_0 = 288$ K and constant stability with $N = 0.01$ s⁻¹ everywhere. A constant horizontal wind $u = 10$ m s⁻¹ is prescribed at the inlet boundary.

Discretisation

The test uses the discretisation of the Euler equations described in section 3.2. The domain is discretised on a grid having 600×100 cells such that $\Delta x = 0.5$ km and $\Delta z = 300$ m. Sponge layers are added to the upper 10 km and leftmost 10 km at the inlet boundary to damp the reflection of waves. The term $\mu \rho \mathbf{u}$ is subtracted from the momentum equation (equation 3.1a) where the damping function μ is adapted from Melvin et al. (2010) such that

$$\mu(x, z) = \mu_{\text{upper}} + \mu_{\text{inlet}} \quad (4.15)$$

$$\mu_{\text{upper}}(z) = \begin{cases} \bar{\mu} \sin^2\left(\frac{\pi}{2} \frac{z - z_B}{H - z_B}\right) & \text{if } z \geq z_B \\ 0 & \text{otherwise} \end{cases} \quad (4.16)$$

$$\mu_{\text{inlet}}(x) = \begin{cases} \bar{\mu} \sin^2\left(\frac{\pi}{2} \frac{x_I - x}{x_I - x_0}\right) & \text{if } x < x_I \\ 0 & \text{otherwise} \end{cases} \quad (4.17)$$

where $\bar{\mu} = 1.2$ is the damping coefficient, $z_B = 20$ km is the bottom of the sponge layer, $H = 30$ km is the top of the domain, $x_0 = -150$ km is the leftmost limit of the domain and $x_I = -140$ km is the

rightmost extent of the inlet sponge layer. The sponge layer is only active on faces whose normal is vertical so that it damps vertical momentum only.

Note that, while the domain itself is 30 km in height, for the purposes of generating of BTF and SLEVE grids, the domain height is set to 20 km because the sponge layer occupies the uppermost 10 km.

No normal flow is imposed at the top and bottom boundaries and the outlet is zero gradient. For Exner, hydrostatic balance is prescribed on all boundaries. Following Melvin et al. (2010), the simulation is integrated forward by 5 hours with a timestep $\Delta t = 8$ s.

Analysis

Comparing vertical velocity contours between BTF and SLEVE show few visible differences (figures 4.13a, c). Evanescent waves are visible as dense contours immediately above the mountain ridges and the large-scale hydrostatic waves propagate vertically. We verify the two wave types using the linear theory discussed in section 2.8. The horizontal wavelength between each mountain peak is specified as $\lambda = 4 \times 10^3$ m, so $k = 2\pi/\lambda \approx 1.57 \times 10^{-3} \text{ m}^{-1}$. The condition for evanescent waves is that $|\bar{u}k| \geq N$. Since this test specifies $N = 0.01 \text{ s}^{-1}$ and $\bar{u} = 10 \text{ m s}^{-1}$, we find that the condition is satisfied.

The mountain half-width is specified to be $a = 5 \times 10^3$ m, so the large-scale wavelength is 1×10^4 m and the horizontal wavenumber $k \approx 6.28 \times 10^{-4} \text{ m}^{-1}$. In this case, $|\bar{u}k| < N$, so waves propagate vertically. Hence, we have shown that both propagating and evanescent waves are generated by this particular configuration of stability, wind speed, and mountain profile.

Since the same model was used, vertical velocities match those from Weller and Shahrokhi (2014). Vertical velocities on the SnapCol grid are similar to the terrain following results (figure 4.13e). All three results are in agreement with a semi-implicit, semi-Lagrangian simulation from Melvin et al. (2010) (see figure 4.13b).

Examining the velocity vector field we find that the flow is qualitatively similar between the BTF grid (figure 4.14a), SnapCol grid (figure 4.14b), and SLEVE grid (not shown). Flow near the ground follows the terrain, accelerating as it passes over the mountain peaks, with velocities becoming more horizontal aloft.

As shown in figures 4.15a, c and e, divergence in the velocity field was found to be negligible everywhere except the lowest layer on all grids. Magnitude of divergence is slightly greater on the SnapCol grid.

Potential temperature anomalies are similar on all grids, having a similar shape to vertical velocity contours (SLEVE grid figure 4.13d, SnapCol grid figure 4.13f, BTF grid not shown). As predicted by the gravity wave theory discussed in section 2.8, potential temperature and vertical velocity anomalies are out of phase by 90° .

Examining more closely the potential temperature anomaly on the SnapCol grid, in the lee of the mountain the bottommost layer is anomalously warm and the layer above it is anomalously cold (figure 4.16b). Potential temperature increases with height because the simulated atmosphere is stable, so these anomalies serve to reduce the stability near the ground. The anomalies are not sufficiently

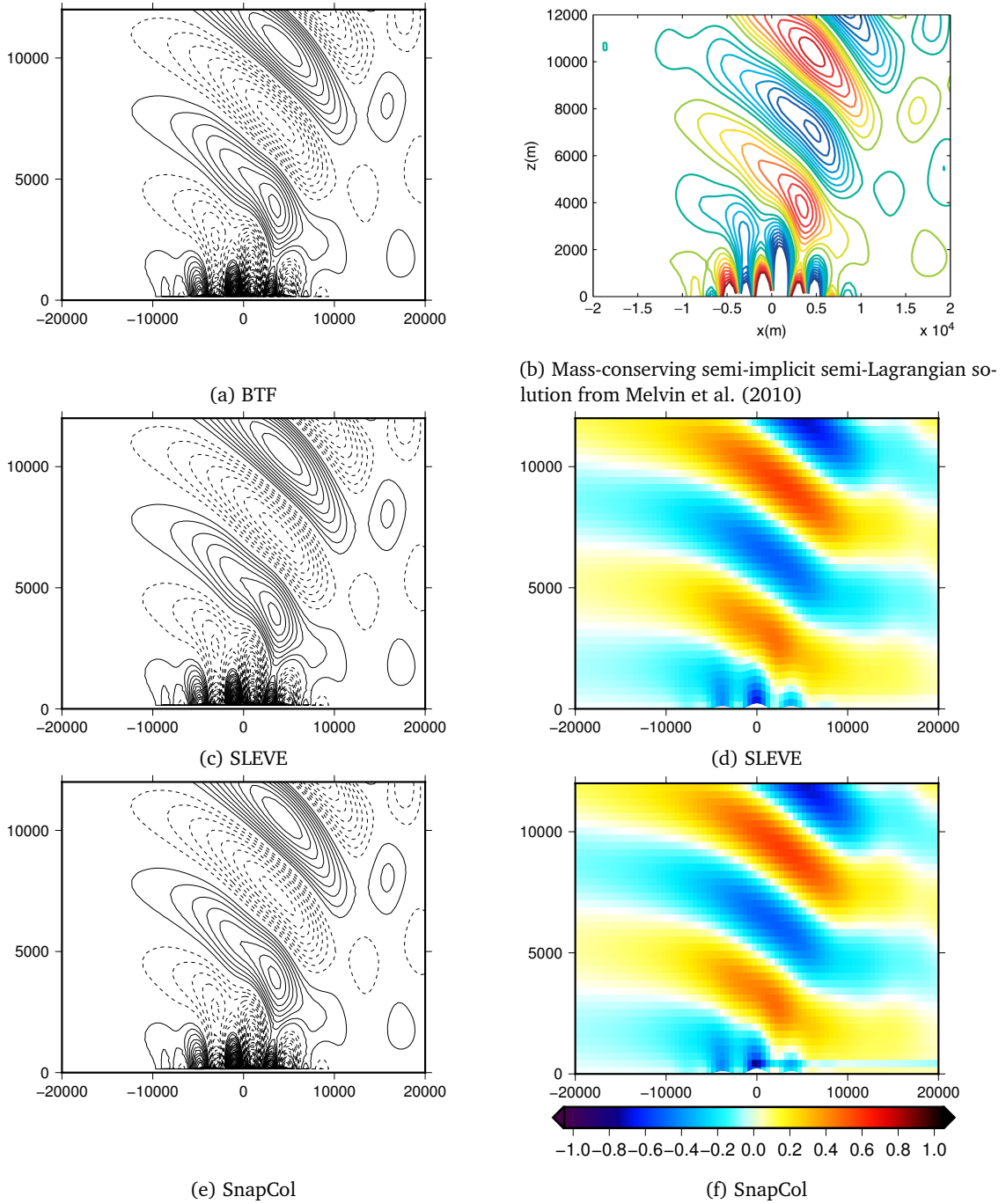


Figure 4.13: Vertical cross section of vertical velocity contours (a, c and e) and potential temperature anomalies in Kelvin (d and f) from the gravity waves test after 5 hours. Vertical velocity contours are every $5 \times 10^{-2} \text{ m s}^{-1}$ with solid lines denoting ascent and dashed lines descent.

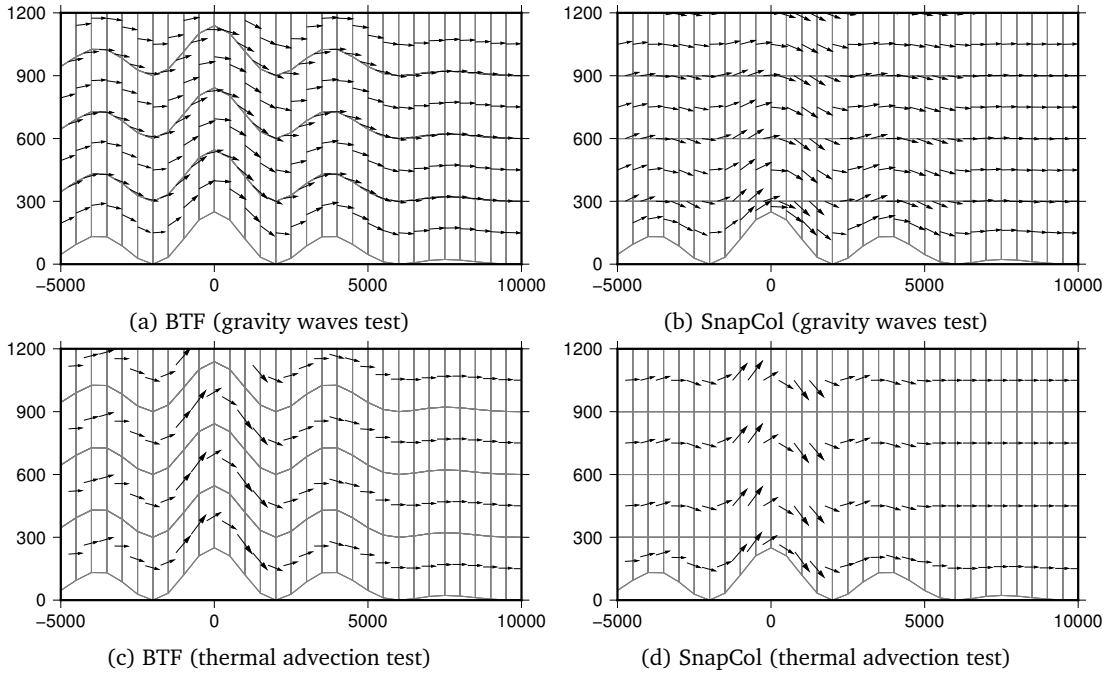


Figure 4.14: Vertical cross section of velocity vectors in the centremost 10 km and lowest 1.2 km. In the gravity waves test, the velocity field after 5 hours follows the terrain and is qualitatively similar on (a) the BTF grid, (b) the SnapCol grid, and the SLEVE grid (not shown). For the thermal advection test described in section 4.5, the terrain following velocity field is prescribed. It is designed to imitate the velocity field of the gravity waves test, and is shown here on the BTF grid (c) and SnapCol grid (d).

large to destabilise the atmosphere, however. Therefore, vertical motion is not expected, and was not observed, near the ground on the lee side. Whilst turbulent motion does cause thermal mixing in the real atmosphere, there is no viscosity in the model equations, so the thermal anomalies should not be present. The feature is not present on the SLEVE grid (figure 4.16a) or BTF grid (not shown).

Figure 4.17a plots vertical profiles of Exner and potential temperature in the lowest 1 km in the lee of the mountain at $x = 50$ km. The Exner function decreases linearly and is identical on BTF and SnapCol grids. The potential temperature profile is linear on the BTF grid but a slight zig-zag is present on the SnapCol grid in the lowest two layers, corresponding to the warm and cold anomalies. This profile shares the same shape as the example presented in figure 2.5. This implies that the computational mode of the Lorenz vertical staggering has been excited, because the zig-zag is present in the potential temperature profile, but not in the Exner profile.

Another test was performed in which the mountain height was doubled such that $h_0 = 500$ m, with all other parameter values unchanged. Divergence of the velocity field was visually unchanged on the BTF grid (figure 4.15b), but magnitude of divergence increased above the mountain peaks on the SLEVE and SnapCol grids (figures 4.15d and 4.15f respectively). Overall potential temperature anomalies increase in magnitude because the gravity wave amplitude is larger, but these waves do not reach all the way to the ground. In the lowest two layers, results on the SLEVE grid are similar for both

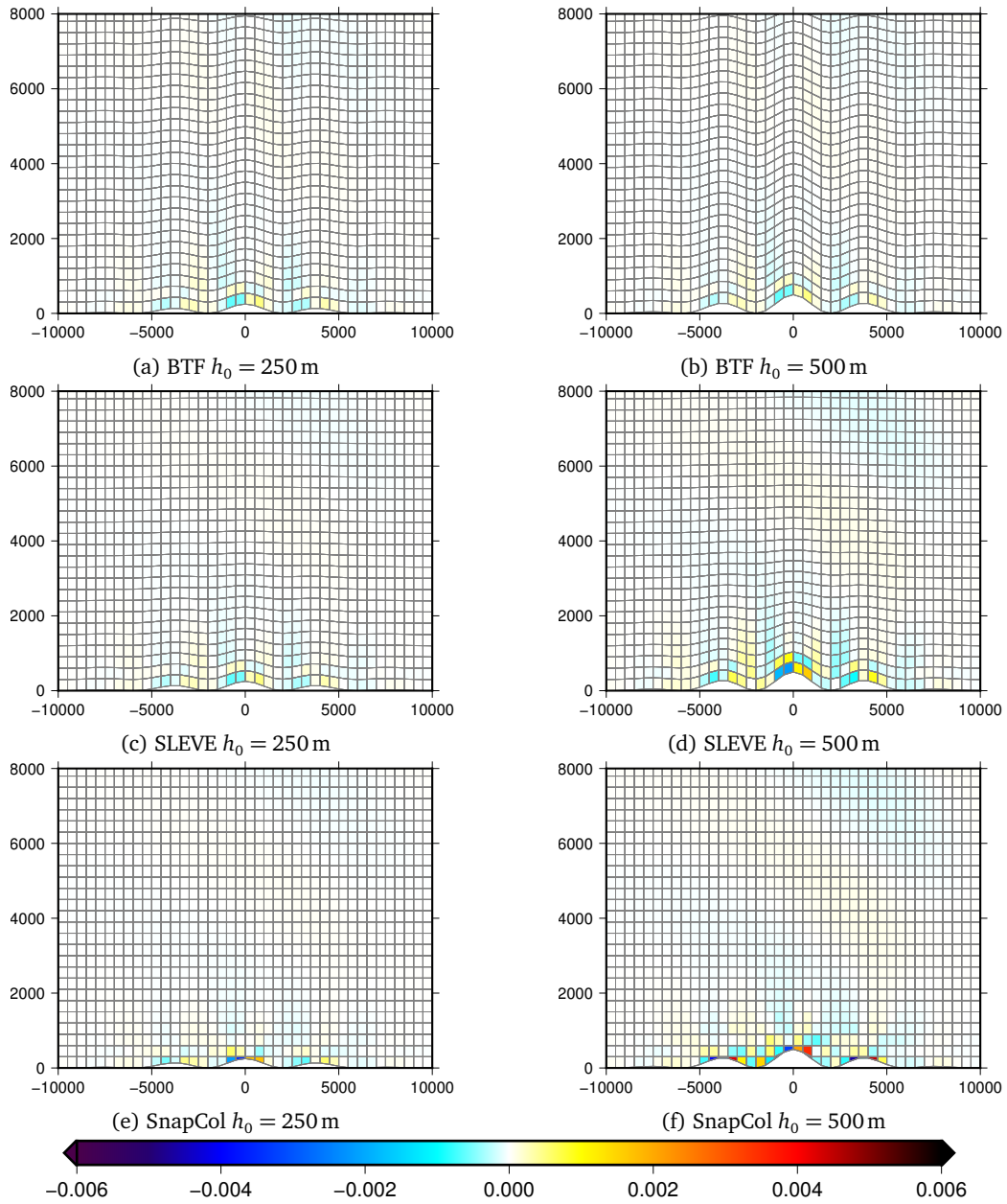


Figure 4.15: Divergence (s^{-1}) of the discrete velocity field for the gravity waves test in the centremost 20 km and lowest 8 km for a mountain height of $h_0 = 250$ m on the BTF grid (a), SLEVE grid (c), and SnapCol grid (e), and for a mountain height of $h_0 = 500$ m on the BTF, SLEVE and SnapCol grids (b, d and f respectively).

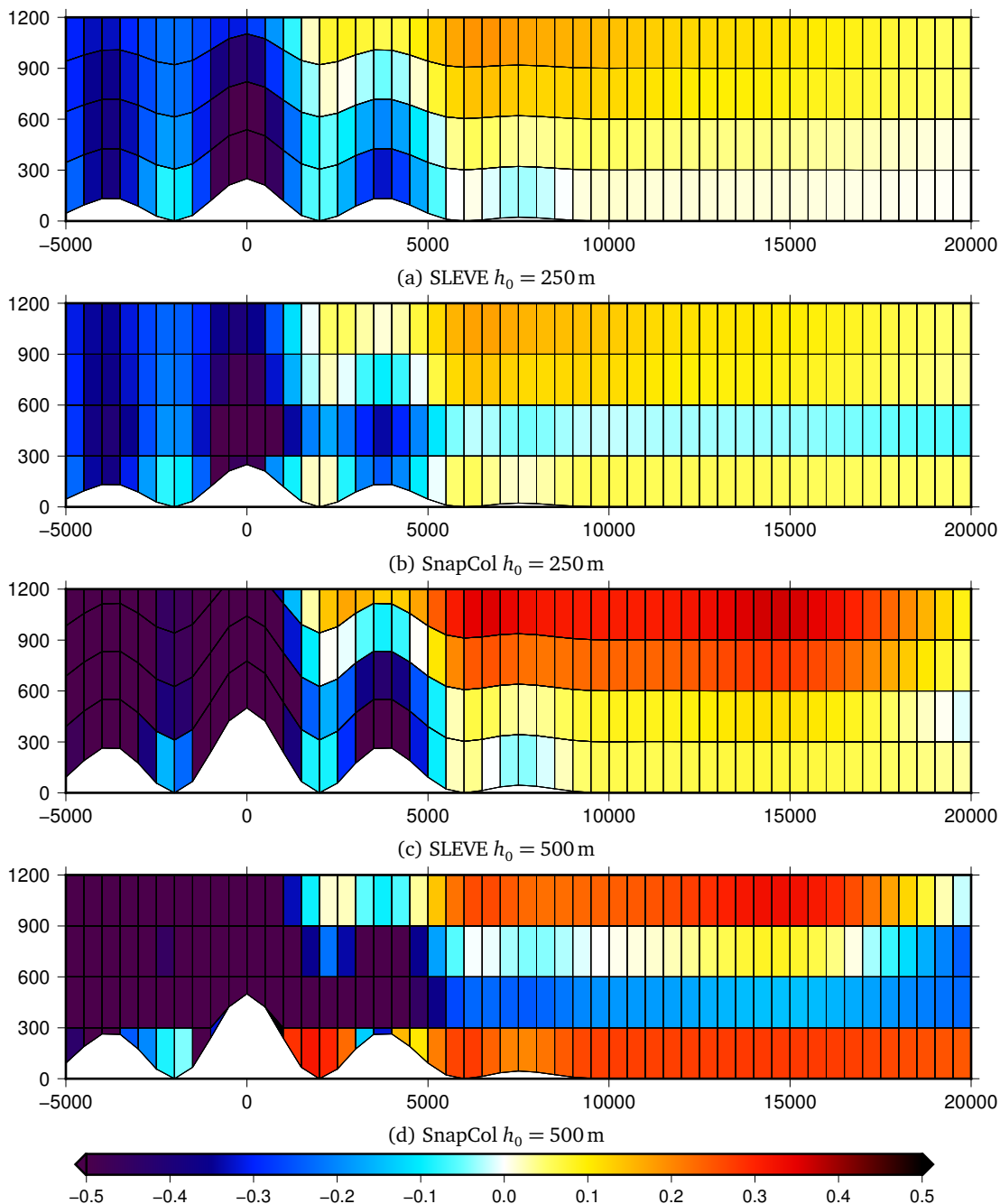


Figure 4.16: Vertical cross section of potential temperature anomalies (K) in the centermost 10 km and lowest 1.2 km after 5 hours. Subfigures (a) and (b) show close up views of the potential temperature anomalies in figures 4.13d and 4.13f respectively. Note the different colour scale from figure 4.13.

Height (m)	Gravity waves, $h_0 = 250$ m			Gravity waves, $h_0 = 500$ m			Thermal advection	
	BTF	SLEVE	SnapCol	BTF	SLEVE	SnapCol	BTF	SnapCol
150	-0.003	-0.001	0.046	-0.003	0.031	0.254	-0.001	-0.643
450	0.006	0.013	-0.05	0.006	0.012	-0.169	0.002	0.652
750	0.032	0.03	0.023	0.032	0.055	-0.169	-0.003	-0.033
1050	0.046	0.04	0.041	0.046	0.106	0.069	0.004	-0.031

Table 4.2: Difference in potential temperature (K) from the initial profile in the lowest 1200 m at $x = 50$ km for the gravity waves test (section 4.4) and thermal advection test (section 4.5).

mountain heights (see figures 4.16a and 4.16c). On the SnapCol grid, the Lorenz computational mode is more severe. Figure 4.17a also shows that potential temperature errors are no longer confined to the lowest two layers, but extend beyond 1200 m above the ground. Differences in potential temperature from the initial profile are summarised in table 4.2.

In section 4.2, we found that errors were largest when advecting a tracer over the SnapCol grid in a terrain following velocity field. This suggests that the computational mode is excited by errors in the upwind-biased advection scheme. A further experiment is presented in section 4.5 to test this hypothesis.

Little evidence of the ‘small cell’ problem associated with cut cell grids, discussed in section 2.4, was found on the SnapCol grid. At each timestep, the maximum and mean Courant number for all cells in the grid was calculated. Whilst initially larger on the SnapCol grid, the maximum Courant number eventually converges for all three grids (figure 4.18a). After 5 hours, the maximum Courant number gradually rises (not shown). In figure 4.18b, we see that the mean Courant number is similar across all grids, but also increases slowly throughout the simulation. It is likely that this is because the gravity waves are still amplifying, leading to a steady increase in wind speeds.

The lack of evidence for the small cell problem be explained by considering flow through a two-dimensional, rectangular cell in the $x-z$ plane in which Δx is several times larger than Δz (figure 4.19). Using equation 3.13 and assuming a uniform flow $\mathbf{u} = (u, 0, w)^T$, the Courant number is

$$Co = \frac{\Delta t}{\Delta x \Delta z} (u \Delta z + w \Delta x) \quad (4.18)$$

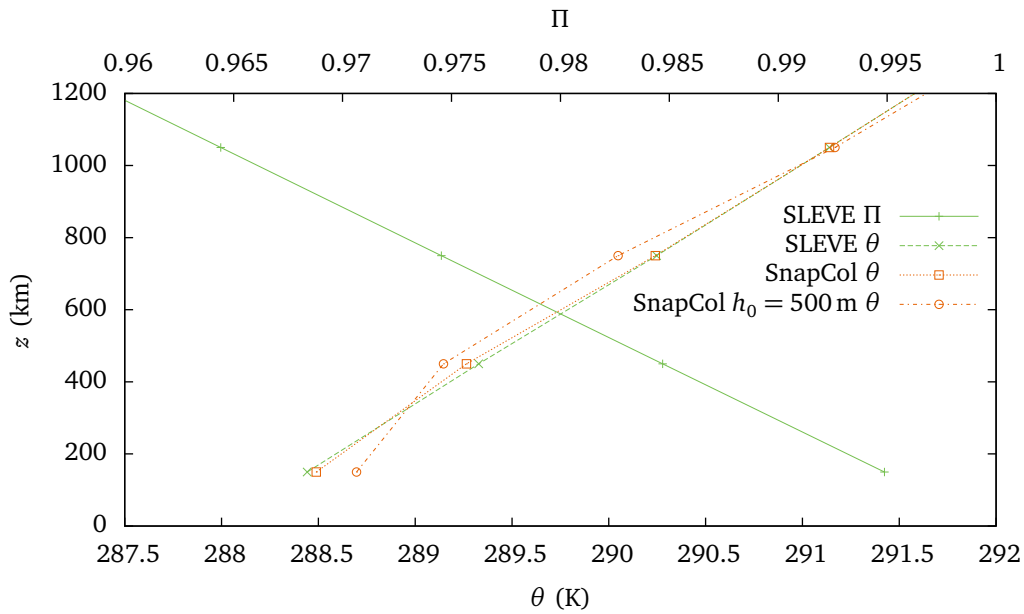
When the flow is almost horizontal, $u \gg w$, so

$$Co \approx \frac{u \Delta t}{\Delta x} \quad (4.19)$$

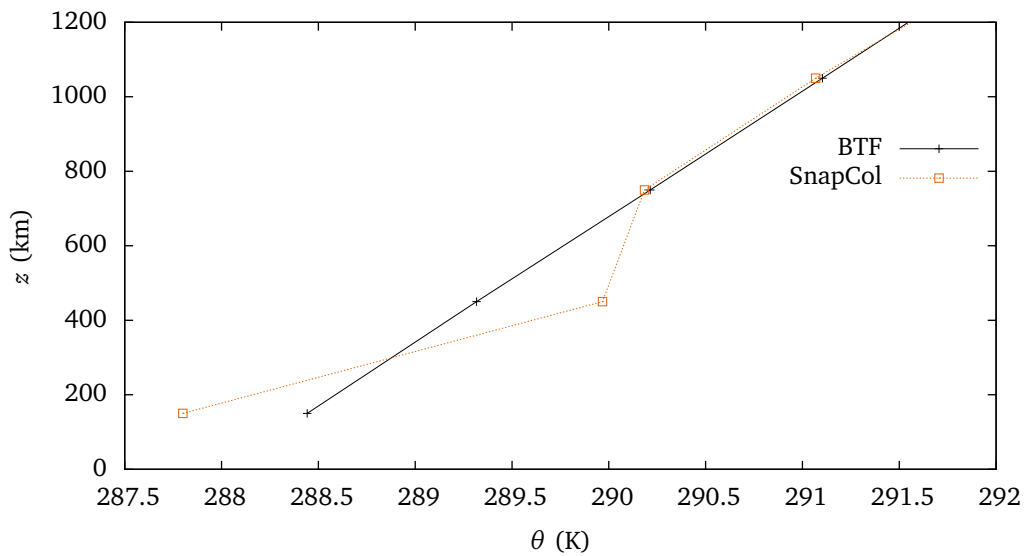
That is, the two-dimensional Courant number reduces to the one-dimensional Courant number. Hence, the cell height Δz has little effect on the CFL criterion.

In the gravity waves test, vertical motion is induced by the terrain and, for the shallow gradients used in this test, horizontal velocities dominate.

In conclusion, test results were similar on all grids and vertical velocities are in good agreement with results from the literature. On the SnapCol grid, thin cells had little effect on the timestep because the flow was predominantly horizontal. Errors in potential temperature were found near the ground in



(a) Vertical profiles of the Exner function of pressure, Π , and potential temperature, θ , in the gravity waves experiment. Exner profile is visually identical on all grids for both $h_0 = 250$ m and $h_0 = 500$ m; for clarity, the Exner profile is only plotted for the SLEVE grid. The computational mode is manifested as a zig-zag in potential temperature on the SnapCol grid. The double height mountain increases the severity of the computational mode, but has negligible effect on the SLEVE grid (not shown). All results on the BTF grid are qualitatively the same as those on the SLEVE grid (not shown).



(b) Vertical potential temperature profile from the test of terrain following advection of a stable thermal profile, described in section 4.5. Results on the BTF grid are visually identical to the initial potential temperature profile (not shown).

Figure 4.17: Vertical profiles in the lowest 1 km in the lee of the mountain at $x = 50$ km after 5 hours.

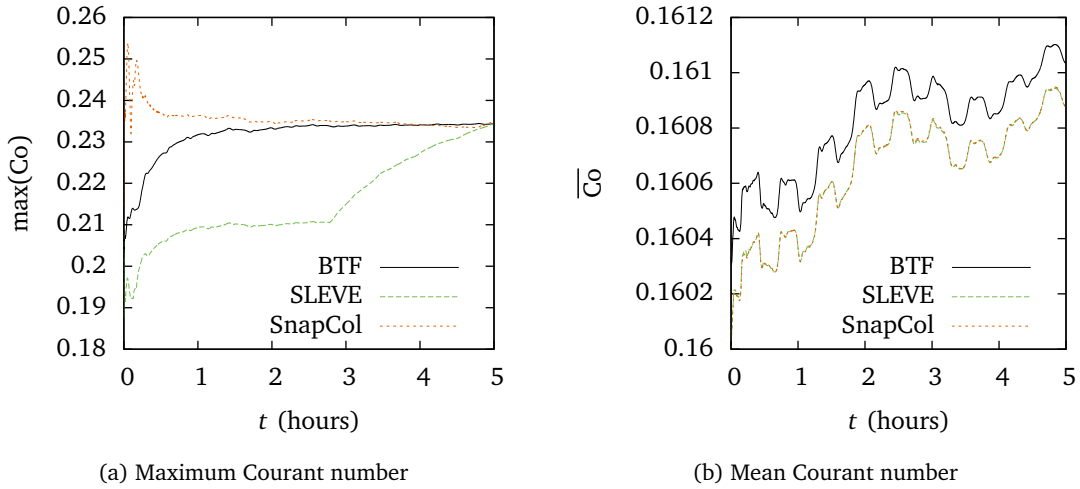


Figure 4.18: Courant numbers on BTF, SLEVE and SnapCol grids for the gravity waves test.

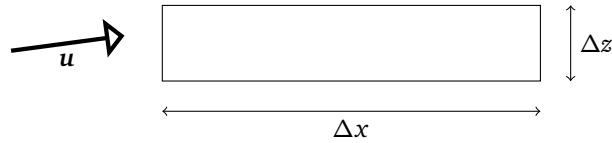


Figure 4.19: Nearly-horizontal flow through a thin, rectangular cell in the $x-z$ plane. Because the vertical velocity component is small, the cell height Δz has a negligible effect on the two-dimensional Courant number.

the lee of the mountain on the SnapCol grid and these were attributed to the Lorenz computational mode. It is possible that regions of relatively large divergence and convergence immediately above the ground are a cause of these thermal errors. Alternatively, the errors may be due to the inaccurate advection of potential temperature, and this possibility is explored in the next test.

4.5 Terrain following advection of a stable thermal profile

This test is designed to investigate the cause of the potential temperature errors found in the gravity waves test. The same potential temperature profile from the gravity waves test is advected over BTF and SnapCol grids using a terrain following velocity field that imitates a physical flow over orography.

Specification

The spatial domain, mountain profile and potential temperature profile are the same as those from the gravity waves test. The potential temperature profile is fixed at the inlet and zero gradient at the outlet boundary so that it is advected consistently. The upwind-biased advection scheme is used, as described in section 3.2. Following the gravity waves test, the model is integrated forward by 5 hours with a timestep $\Delta t = 8$ s.

The velocity field is given by equation 4.11 but, because the mountain profile is different, the derivative of terrain height, $\partial h/\partial x$, is

$$\frac{\partial h}{\partial x} = -2h_0 \exp\left(-\left(\frac{x}{a}\right)^2\right) \cos\left(\frac{\pi x}{\lambda}\right) \left[\frac{\pi}{\lambda} \sin\left(\frac{\pi x}{\lambda}\right) + \frac{x}{a^2} \cos\left(\frac{\pi x}{\lambda}\right) \right] \quad (4.20)$$

Analysis

The velocity field is shown on both BTF and SnapCol grids (figures 4.14c and 4.14d) for comparison with the velocity field from the gravity waves test (figures 4.14a and 4.14b). The prescribed flow is qualitatively similar to the flow in the gravity waves test. However, because the velocity field follows the terrain, vertical velocities are stronger in areas of steep terrain in the thermal advection test. A quantitative comparison would require all velocities to be defined at cell faces, and this is the subject of further work discussed in section 6.1.

Divergence was calculated for the velocity fields, but, unlike the results in the gravity waves test (see figure 4.15), it was found to be negligible on both grids in this thermal advection test (not shown).

Potential temperature anomalies after 5 hours on the BTF and SnapCol grids are shown in figure 4.20. On both grids, columns of lower potential temperature are seen above the mountain peaks, due to the orographic lifting of air at the ground. Hence, the highest central peak produces the largest cold anomaly. Similarly, on both grids, a warm anomaly is found near the outlet (not shown). It is created by high potential temperature initially above the mountain peaks being advected down to the ground.

Similar to the gravity waves result, on the SnapCol grid, potential temperature anomalies are found near the ground in the lee of the mountain (see figure 4.20b). Importantly, however, the anomalies are reversed when compared to the result from the gravity waves test in figure 4.13f: in this advection test, the layer nearest the ground is anomalously cold and the layer above it is anomalously warm. This error structure could not cause the thermal errors found in the gravity waves test.

Vertical profiles of potential temperature on the BTF and SnapCol grids are presented in figure 4.17b, for comparison with the same profiles from the gravity waves test in figure 4.17a. Differences in potential temperature from the initial profile are compared to the results from the gravity waves test in table 4.2.

Given that the potential temperature anomalies are inverted compared to the gravity waves test, it is not certain that the Lorenz computational mode is excited by advection errors, although this is still a possible cause.

It is important to note two differences between the gravity waves test and this advection test. First, only the advection equation is being solved instead of the fully-compressible Euler equations that were solved in the gravity waves test. Second, the velocity field that is prescribed does not match exactly the flow in the gravity waves test, and this was evidenced by the decreased divergence in this thermal advection test. Improvements to the velocity field are proposed in section 6.3.

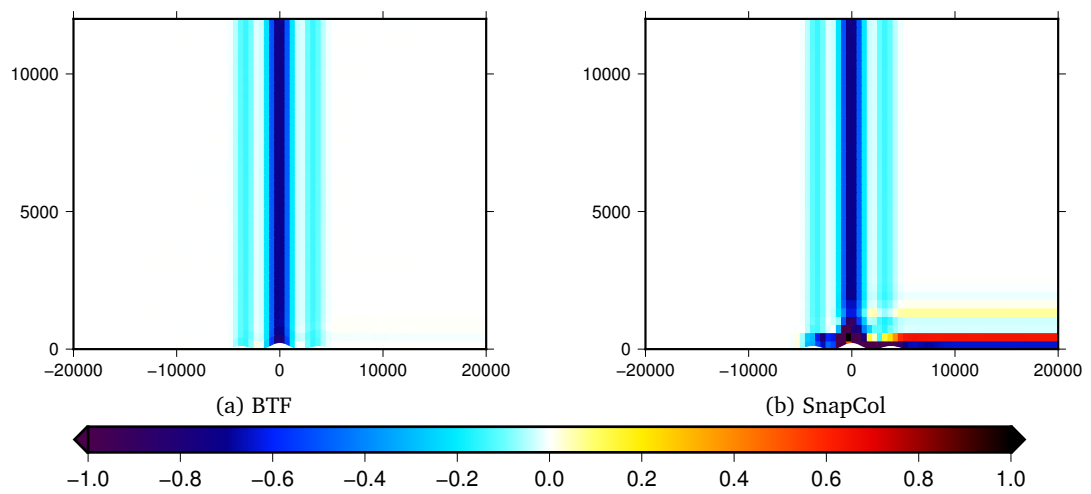


Figure 4.20: Potential temperature anomalies of terrain following advection of a stable potential temperature profile at $t = 18000$ s.

5 Conclusions

This project has compared BTF and SLEVE terrain following grids with the ‘SnapCol’ grid which approximates a piecewise linear cut cell grid. Numerical errors have been analysed for a variety of two-dimensional test cases, solving the fully-compressible Euler equations and the linear advection equation.

The model’s upwind-biased cubic advection scheme, introduced in section 3.2, was tested in the horizontal advection of a tracer in section 4.1. Tracer shape was maintained on all grids and tracer magnitude was well-preserved on all except the BTF grid. In line with existing studies, the most accurate results were found on the SnapCol grid, having errors comparable to those on a regular grid without orography. Errors were largest on the BTF grid, with artefacts remaining above the mountain, and mild distortion as the tracer passed over the mountain, though accuracy was nevertheless better than the BTF result from Schär et al. (2002). Divergence in the discrete velocity field was found on the BTF grid in the region of vertical wind shear which accounted for the artefacts above the mountain.

In section 4.2, a second advection test was designed to determine if advection errors are caused by non-uniformity and skewness, or by misalignment of the flow with grid layers. To this end, a velocity field was formulated that follows the layers of the BTF grid. Errors on the BTF grid were greatly reduced, but the result on the SnapCol grid was the worst of all the tracer advection tests with tracer magnitude significantly reduced. Therefore, we conclude that advection errors are caused by flow crossing grid layers, since accuracy was greatest on the non-orthogonal BTF grid. The lack of monotonicity of the advection scheme motivates the introduction of a flux limiter, and this is discussed in section 6.1.

A test of a mountain profile submerged in a resting atmosphere was presented in section 4.3. It was designed to test the accuracy of non-orthogonal calculations of momentum, which is especially challenging on the more non-orthogonal terrain following grids. Spurious motion was found to be small on all grids. Spurious vertical velocities on the SLEVE grid were comparable to the same result from Schär et al. (2002), but offered only a small improvement compared to the BTF grid. Vertical velocity was reduced by almost three orders of magnitude on the SnapCol grid. Spurious velocities on the regular grid were still higher than the result on a cut cell grid from Good et al. (2014), and this is the subject of further work in section 6.2.

Energy was well-conserved on all grids with energy slowly decreasing on the SnapCol grid and a

regular grid with flat terrain. However, periods of energy gain were found on BTF and SLEVE grids. Diagnosing the source of these energy increases will require further work.

In section 4.4, orographically induced gravity waves were modelled. Velocity fields were qualitatively very similar across all grids, and vertical velocity contours agreed with the mass-conserving semi-implicit semi-Lagrangian result from Melvin et al. (2010). Little evidence of the ‘small cell’ problem was found and we argue that, because the flow is mainly horizontal, this has negligible effect on the Courant number in thin cells.

Potential temperature anomalies in the gravity waves test were also visually similar across all grids, except near the ground in the lee of the mountain on the SnapCol grid. Potential temperatures were anomalously high in the lowest layer, and anomalously low in the layer immediately above, whilst no such anomalies were present in the Exner profile. This is a typical manifestation of the Lorenz computational mode in which discrete hydrostatic balance is preserved despite a ‘zig-zag’ in potential temperature. The magnitude of these anomalies increased on the SnapCol grid when the mountain height was doubled, but results on the TF grids were largely unaffected. Divergence and convergence in the discrete velocity field was found in cells located next to mountain peaks.

We offer three possible causes of the computational mode. First, although velocity fields were visually similar on all grids, errors may exist in the velocity field on the SnapCol grid. Second, it may be that the velocity field is reasonable, but that potential temperature is advected wrongly on the SnapCol grid. Third, we posit that, because the magnitude of divergence was greatest on the SnapCol grid, divergence in the discrete velocity field plays a role in exciting the computational mode.

A final test was designed to investigate the cause of these potential temperature anomalies (section 4.5). We hypothesised that errors in the advection scheme excited the Lorenz computational mode. The same thermal profile was advected using a terrain following velocity field that imitates the velocity field in the gravity waves test. The velocity field is visually similar to those from the gravity waves test, although vertical velocities are larger in the thermal advection test.

Once again, potential temperature anomalies were found in the lowest two layers in the lee of the mountain. However, in this advection test, the anomalies were reversed with the anomalously low potential temperatures in the lowest layer. It is possible that the structure of errors differ because the flow prescribed in the thermal advection test does not imitate the gravity waves velocity field closely enough. Further tests are required to be certain of the cause of the Lorenz computational mode, and this is discussed in section 6.3.

6 Further work

The results of the five experiments from chapter 4 motivate several routes of further work. Before discussing these, however, we identify three other items worthy of study.

First, in order to compare results with those from other experiments, such as Good et al. (2014), the SnapCol grid should be improved so that all cut cells are aligned in rows and columns. As discussed in section 3.1, some cells that intersect the surface are slightly distorted during the construction of the SnapCol grid.

Second, all experiments were performed on in Cartesian coordinates and, unlike most existing implementations of terrain following layers, no coordinate transform was used. We should investigate the metric terms introduced by terrain following coordinates, and determine whether a discretisation with metric terms can be mathematically equivalent to the Cartesian coordinate discretisation.

Third, it is desirable to perform additional verification of the model of Weller and Shahrokhi (2014) using idealised simulations on regular grids without orography. Following the set of test cases for nonhydrostatic models proposed by Skamarock et al. (2004), two further tests might be undertaken. First, following Skamarock and Klemp (1994), a simulation of the evolution of gravity waves from a potential temperature anomaly in a stable atmosphere with a horizontal wind. Second, following Straka et al. (1993), a cold bubble sinks to the ground, creating a density current that travels horizontally. Results of both tests should be compared with reference solutions from Skamarock and Klemp (1994) and the results of Jebens et al. (2011).

6.1 Advection scheme

For the three advection tests described in sections 4.1, 4.2 and 4.5, the standard OpenFOAM advection solver was used, which has two shortcomings. First, whilst advection is treated explicitly in the fully-compressible model from Weller and Shahrokhi (2014), the scalar transport model solves the advection equation (equation 4.6) using implicit time-stepping. Second, the velocity fields for the three advection tests had velocities stored at cell centres. The scalar transport model introduces additional error when velocities are linearly interpolated onto cell faces during model initialisation¹.

¹For details, refer to <https://github.com/OpenFOAM/OpenFOAM-2.3.x/blob/9fd0db/src/finiteVolume/cfdTools/incompressible/createPhi.H>

To avoid these two issues, a custom scalar transport model should be implemented that solves the advection equation explicitly and accepts a field in which velocities are defined at cell faces. This has the added advantage that any velocity field from any fully-compressible simulation, such as the gravity waves test from section 4.4, can be used as the prescribed velocity field for an advection test.

The upwind-biased cubic advection scheme, described in section 3.2, is not monotonic. Results from horizontal and terrain following tracer advection tests showed that minimum and maximum tracer values decreased over time (see sections 4.1 and 4.2). In similar tracer advection experiments, Jones (2013) found that the van Leer scheme gave most accurate results. The scheme is designed to maximise boundedness and accuracy, blending a centred difference scheme that is second-order accurate and unbounded with an upwind scheme that is first-order accurate and bounded. This motivates the development of a monotonicity preserving version of the upwind-biased cubic advection scheme. Due to its larger stencil size, we would expect such a scheme to have greater accuracy compared to the current upwind-biased scheme, and the van Leer scheme used by Jones (2013).

In the horizontal advection test, we identified that divergence in the discrete velocity field on the BTF grid is a source of error in tracer magnitude in the region of vertical wind shear. We propose a new test that would help quantify the error contribution due to divergence. Here, the discrete velocity field should be made non-divergent by using Chorin's method to project onto a divergence-free space (Chorin 1968).

Results from horizontal and terrain following tracer advection tests also showed that accuracy was greatest when the velocity field was aligned with the grid. This motivates further tests using an adaptive mesh that is dependent upon the flow. An adaptive mesh redistribution technique might be employed such as the three dimensional formulation by Browne et al. (2014).

6.2 Resting atmosphere errors

Three findings from the resting atmosphere test (section 4.3) have yet to be understood. First, compared to the results of Good et al. (2014), the maximum vertical velocity on a regular grid is larger than expected (figure 4.10a) which may be due to loss of precision when loading the initial conditions. Second, computational oscillations in vertical velocity were found on the BTF grid which eventually lead to numerical instability (not shown). This error has not been seen on any other grid, nor in any other test case. Third, whilst total energy gradually decreased on the SnapCol and regular grids, some energy gain was seen on the BTF and optimised SLEVE grids. Given that energy continued to increase on the BTF grid, we would expect this to contribute to the numerical instability.

Therefore, further work is required using longer integration times to diagnose the errors in this test and, in particular, more effort is needed to understand the lack of energy conservation. Additionally, two more resting atmosphere tests should be carried out. First, the mountain height should be increased from 1 km to 4 km for comparison with results from Zängl (2012) and Good et al. (2014). Second, a test of a neutrally stable atmosphere at rest by Botta et al. (2004) found that errors were close to machine precision but that errors increased when stratification was included. Comparisons with this test would be useful to further explore the sources of numerical error in idealised resting atmospheres.

6.3 Gravity waves and potential temperature errors

The results of terrain following advection of a thermal profile (section 4.5) showed a different potential temperature error structure compared to those on the SnapCol grid in the gravity waves test (section 4.4). These results could be different because the velocity fields in the two tests are not the same.

Instead of prescribing an idealised velocity field, a further advection test might be developed that uses a velocity field more similar to the gravity waves simulation. The gravity waves velocity field on the BTF grid might be taken as the prescribed velocity field in the new advection test. The custom transport model, discussed earlier in this chapter, would make this straightforward on the BTF grid. However, velocities would have to be interpolated from the BTF grid onto the SnapCol grid. We could not simply prescribe the SnapCol velocity field from the gravity waves test because the velocity field itself may contain errors.

By using a more physical velocity field we hope that the new advection test would produce the same potential temperature error structure as the errors on the SnapCol grid in the gravity waves test. This result would confirm that the Lorenz computational mode is excited by errors in the advection of potential temperature.

To further investigate the Lorenz computational mode found on the SnapCol grid in the gravity waves test, a Charney–Phillips staggering should be formulated and implemented for unstructured grids. We hypothesise that the potential temperature errors near the ground on the lee slope would be reduced on a Charney–Phillips grid since stationary oscillations in the potential temperature field would not be maintained.

Little evidence of the small cell problem was found in the gravity waves test. The Courant number was shown to be independent of horizontal velocity and, because flow is near-horizontal in the gravity waves test, there was no small cell problem. To confirm this hypothesis, another test might be constructed in which a cold thermal anomaly descends onto a mountain. This test is similar to the density current test case from Straka et al. (1993), but includes a mountain profile. The vertical momentum that reaches the surface should, for a sufficiently large timestep, cause numerical instability on the SnapCol grid but a stable solution on terrain following grids. This would motivate the merging of small cells following Yamazaki and Satomura (2010).

All tests presented in this project use one of two wave-shaped mountain profiles (given by equations 4.1 and 4.13). Many experiments on cut cell grids perform simulations over bell-shaped mountain profiles known as ‘Witch of Agnessi’ (Steppeler et al. 2002; Rosatti et al. 2005; Klein et al. 2009; Jebens et al. 2011). Following Gallus and Klemp (2000), a further test should be developed to simulate flow over a the bell-shaped mountain profile to allow comparison with existing results.

Lock et al. (2012) extended the two-dimensional test from Gallus and Klemp (2000) to simulate flow over a three dimensional mountain, presenting results on a cut cell grid. It would be valuable to compare model results for terrain following and cut cell grids in three dimensions.

Bibliography

- Adcroft, A., C. Hill and J. Marshall, 1997: Representation of topography by shaved cells in a height coordinate ocean model. *Mon. Wea. Rev.*, **125**, 2293–2315.
- Apostol, T. M., 1969: *Calculus. Multi-Variable Calculus and Linear Algebra with Applications to Differential Equations and Probability*. 2nd ed. Vol. 2. John Wiley & Sons, Ltd. 673 pp.
- Arakawa, A. and C. S. Konor, 1996: Vertical Differencing of the Primitive Equations Based on the Charney-Phillips Grid in Hybrid σ - p Vertical Coordinates. *Mon. Wea. Rev.*, **124**, 511–528.
- Arakawa, A. and S. Moorthi, 1988: Baroclinic instability in vertically discrete systems. *J. Atmos. Sci.*, **45**, 1688–1708.
- Barry, R. G., 2008: *Mountain Weather and Climate*. 3rd ed. Cambridge University Press. 532 pp.
- Blaise, S. and A. St-Cyr, 2012: A Dynamic hp -Adaptive Discontinuous Galerkin Method for Shallow-Water Flows on the Sphere with Application to a Global Tsunami Simulation. *Mon. Wea. Rev.*, **140**, 978–996.
- Botta, N., R. Klein, S. Langenberg and S. Lützenkirchen, 2004: Well balanced finite volume methods for nearly hydrostatic flows. *J. Comp. Phys.*, **196**, 539–565.
- Browne, P., C. Budd, C. Piccolo and M. Cullen, 2014: Fast three dimensional r-adaptive mesh redistribution. *J. Comp. Phys.*, **275**, 174–196.
- Charney, J. G. and N. A. Phillips, 1953: Numerical integration of the quasi-geostrophic equations for barotropic and simple baroclinic flows. *J. Meteor.*, **10**, 71–99.
- Chorin, A. J., 1968: Numerical solution of the Navier–Stokes equations. *Math. Comput.*, **22**, 745–762.
- Cullen, M. et al., 1997: An Overview of Numerical Methods for the Next Generation U.K. NWP and Climate Model. *Atmosphere-Ocean*, **35**, 425–444.
- Curry, J. A. and P. J. Webster, 1998: *Thermodynamics of Atmospheres and Oceans*. Vol. 65. Academic Press. 471 pp.
- Dempsey, D. and C. Davis, 1998: Error analyses and test of pressure gradient force schemes in nonhydrostatic, mesoscale model. *12th Conf. on Numerical Weather Prediction*, Phoenix, AZ. Amer. Meteor. Soc., 236–239.
- Eliassen, A., 1949: The Quasi-Static Equations of Motion with Pressure as Independent Variable. *Geophys. Publ.*, **17**, 5–17.

- Gal-Chen, T. and R. C. Somerville, 1975: On the Use of a Coordinate Transformation for the Solution of the Navier-Stokes Equations. *J. Comp. Phys.*, **17**, 209–228.
- Gallus, W. A. and J. B. Klemp, 2000: Behavior of Flow over Step Orography. *Mon. Wea. Rev.*, **128**, 1153–1164.
- Gary, J. M., 1973: Estimate of Truncation Error in Transformed Coordinate, Primitive Equation Atmospheric Models. *J. Atmos. Sci.*, **30**, 223–233.
- Good, B., A. Gadian, S.-J. Lock and A. Ross, 2014: Performance of the cut-cell method of representing orography in idealized simulations. *Atmospheric Science Letters*, **15**, 44–49.
- Holdaway, D., J. Thuburn and N. Wood, 2013a: Comparison of Lorenz and Charney–Phillips vertical discretisations for dynamics–boundary layer coupling. Part I: Steady states. *Quart. J. Roy. Meteor. Soc.*, **139**, 1073–1086.
- 2013, b: Comparison of Lorenz and Charney–Phillips vertical discretisations for dynamics–boundary layer coupling. Part II: Transients. *Quart. J. Roy. Meteor. Soc.*, **139**, 1087–1098.
- Holton, J. R., J. A. Curry and J. A. Pyle, 2003: *Encyclopedia of Atmospheric Sciences*. Vol. 3. Academic Press. 2780 pp.
- Jebens, S., O. Knoth and R. Weiner, 2011: Partially implicit peer methods for the compressible Euler equations. *J. Comp. Phys.*, **230**, 4955–4974.
- Jones, M., 2013: Vertical Coordinates Over Orography. M.Sc. Dissertation. University of Reading.
- Klein, R., K. Bates and N. Nikiforakis, 2009: Well-balanced compressible cut-cell simulation of atmospheric flow. *Phil. Trans. R. Soc.*, **367**, 4559–4575.
- Klemp, J. B., 2011: A terrain-following coordinate with smoothed coordinate surfaces. *Mon. Wea. Rev.*, **139**, 2163–2169.
- Klemp, J. B., W. C. Skamarock and O. Fuhrer, 2003: Numerical consistency of metric terms in terrain-following coordinates. *Mon. Wea. Rev.*, **131**, 1229–1239.
- Konor, C. S. and A. Arakawa, 1997: Design of an Atmospheric Model Based on a Generalized Vertical Coordinate. *Mon. Wea. Rev.*, **125**, 1649–1673.
- Leuenberger, D., M. Koller, O. Fuhrer and C. Schär, 2010: A Generalization of the SLEVE Vertical Coordinate. *Mon. Wea. Rev.*, **138**, 3683–3689.
- LeVeque, R. J., 2002: *Finite Volume Methods for Hyperbolic Problems*. Cambridge University Press. 580 pp.
- Lock, S.-J., H.-W. Bitzer, A. Coals, A. Gadian and S. Mobbs, 2012: Demonstration of a Cut-Cell Representation of 3D Orography for Studies of Atmospheric Flows over Very Steep Hills. *Mon. Wea. Rev.*, **140**, 411–424.
- Lorenz, E. N., 1960: Energy and numerical weather prediction. *Tellus*, **12**, 364–373.
- Lott, F. and M. J. Miller, 1997: A new subgrid-scale orographic drag parametrization: Its formulation and testing. *Quart. J. Roy. Meteor. Soc.*, **123**, 101–127.
- Luo, H. and M. Yanai, 1983: The Large-Scale Circulation and Heat Sources over the Tibetan Plateau and Surrounding Areas during the Early Summer of 1979. Part I: Precipitation and Kinematic Analyses. *Mon. Wea. Rev.*, **111**, 922–944.
- Lynch, A. H. and J. J. Cassano, 2006: *Applied Atmospheric Dynamics*. John Wiley & Sons. 290 pp.

- Mahrer, Y., 1984: An Improved Numerical Approximation of the Horizontal Gradients in a Terrain-Following Coordinate System. *Mon. Wea. Rev.*, **112**, 918–922.
- Marshall, J., K. Emanuel and A. Adcroft, 2004: *12.950 Atmospheric and Oceanic Modeling, Spring 2004*. License: Creative Commons BY-NC-SA. URL: <http://ocw.mit.edu/courses/earth-atmospheric-and-planetary-sciences/12-950-atmospheric-and-oceanic-modeling-spring-2004/lecture-notes/lec25.pdf>.
- McFarlane, N., 1987: The effect of orographically excited gravity wave drag on the general circulation of the lower stratosphere and troposphere. *J. Atmos. Sci.*, **44**, 1775–1800.
- Melvin, T., M. Dubal, N. Wood, A. Staniforth and M. Zerroukat, 2010: An inherently mass-conserving iterative semi-implicit semi-Lagrangian discretization of the non-hydrostatic vertical-slice equations. *Quart. J. Roy. Meteor. Soc.*, **136**, 799–814.
- Mesinger, F., 2004: The Eta model: Design, History, Performance, What Lessons have we Learned? *Symposium on the 50th Anniversary of Operational Numerical Weather Prediction*, University of Maryland, MD. Amer. Meteor. Soc., 14–17.
- Mesinger, F., Z. I. Janjić, S. Ničkovic, D. Gavrilo and D. G. Deaven, 1988: The step-mountain coordinate: Model Description and Performance for Cases of Alpine Lee Cyclogenesis and for a Case of an Appalachian Redevelopment. *Mon. Wea. Rev.*, **116**, 1493–1518.
- Moraes, A. d. O. S., P. L. da Cunha Lage, G. C. Cunha and L. F. L. R. da Silva, 2013: Analysis of the non-orthogonality correction of finite volume discretization on unstructured meshes. *22nd International Congress of Mechanical Engineering*, Ribeirão Preto, Brazil. Associação Brasileira de Engenharia e Ciências Mecânicas. URL: www.abcm.org.br/pt/wp-content/anais/cobem/2013/PDF/740.pdf.
- OpenCFD Foundation, 2014a: *OpenFOAM® – Programmer’s Guide*. URL: <http://foam.sourceforge.net/docs/Guides-a4/ProgrammersGuide.pdf>.
- 2014, b: *OpenFOAM® – The Open Source Computational Fluid Dynamics Toolbox*. URL: <http://www.openfoam.org>.
- Pain, C. et al., 2005: Three-dimensional unstructured mesh ocean modelling. *Ocean Modelling*, **10**, 5–33.
- Parkinson, S., J. Hill, M. Piggott and P. Allison, 2014: Direct numerical simulations of particle-laden density currents with adaptive, discontinuous finite elements. *Geosci. Model Dev.*, under review.
- Phillips, N. A., 1957: A coordinate system having some special advantages for numerical forecasting. *J. Meteor.*, **14**, 184–185.
- Ray, P. S., 1986: *Mesoscale Meteorology and Forecasting*. University of Chicago Press. 793 pp.
- Rosatti, G., D. Cesari and L. Bonaventura, 2005: Semi-implicit, semi-Lagrangian modelling for environmental problems on staggered Cartesian grids with cut cells. *J. Comp. Phys.*, **204**, 353–377.
- Schär, C., D. Leuenberger, O. Fuhrer, D. Lüthi and C. Girard, 2002: A new terrain-following vertical coordinate formulation for atmospheric prediction models. *Mon. Wea. Rev.*, **130**, 2459–2480.
- Simmons, A. J. and D. M. Burridge, 1981: An energy and angular-momentum conserving vertical finite-difference scheme and hybrid vertical coordinates. *Mon. Wea. Rev.*, **109**, 758–766.

- Skamarock, W. C., J. Doyle, P. Clark and N. Wood, 2004: A Standard Test Set for Nonhydrostatic Dynamical Cores of NWP Models. *16th Conf. on Numerical Weather Prediction*, Seattle WA. Amer. Meteor. Soc. URL: http://www2.mmm.ucar.edu/projects/srnwp_tests/.
- Skamarock, W. C. and J. B. Klemp, 1994: Efficiency and Accuracy of the Klemp-Wilhelmson Time-Splitting Technique. *Mon. Wea. Rev.*, **122**, 2623–2630.
- Smolarkiewicz, P. K. and J. Szmelter, 2011: A nonhydrostatic unstructured-mesh soundproof model for simulation of internal gravity waves. *Acta Geophysica*, **59**, 1109–1134.
- Steppeler, J., H.-W. Bitzer, M. Minotte and L. Bonaventura, 2002: Nonhydrostatic Atmospheric Modeling using a z -Coordinate Representation. *Mon. Wea. Rev.*, **130**, 2143–2149.
- Steppeler, J., R. Hess, U. Schättler and L. Bonaventura, 2003: Review of numerical methods for nonhydrostatic weather prediction models. *Meteorology and Atmospheric Physics*, **82**, 287–301.
- Steppeler, J. et al., 2006: Prediction of Clouds and Rain Using a z -Coordinate Nonhydrostatic Model. *Mon. Wea. Rev.*, **134**, 3625–3643.
- Straka, J., R. B. Wilhelmson, L. J. Wicker, J. R. Anderson and K. K. Droegemeier, 1993: Numerical solutions of a non-linear density current: A benchmark solution and comparisons. *Int. J. Numer. Methods Fluids*, **17**, 1–22.
- Thuburn, J., C. Cotter and T. Dubos, 2014: A mimetic, semi-implicit, forward-in-time, finite volume shallow water model: comparison of hexagonal-icosahedral and cubed-sphere grids. *Geosci. Model Dev.*, **7**, 909–929.
- Thuburn, J. and C. Cotter, 2012: A framework for mimetic discretization of the rotating shallow-water equations on arbitrary polygonal grids. *SIAM Journal on Scientific Computing*, **34**, B203–B225.
- Weller, H. and A. Shahrokhi, 2014: Curl free pressure gradients over orography in a solution of the fully compressible Euler equations with implicit treatment of acoustic and gravity waves. *Mon. Wea. Rev.*, in preparation.
- Xue, M. and A. J. Thorpe, 1991: A mesoscale numerical model using the nonhydrostatic pressure-based sigma-coordinate equations: Model experiments with dry mountain flows. *Mon. Wea. Rev.*, **119**, 1168–1185.
- Yamazaki, H. and T. Satomura, 2010: Nonhydrostatic Atmospheric Modeling Using a Combined Cartesian Grid. *Mon. Wea. Rev.*, **138**, 3932–3945.
- Ye, D., 1981: Some Characteristics of the Summer Circulation Over the Qinghai-Xizang (Tibet) Plateau and Its Neighborhood. *Bull. Amer. Meteor. Soc.*, **62**, 14–19.
- Zängl, G., 2012: Extending the numerical stability limit of terrain-following coordinate models over steep slopes. *Mon. Wea. Rev.*, **140**, 3722–3733.